UNIVERSITÀ DEGLI STUDI DI PADOVA

Department of Industrial Engineering DII
Master's degree in Aerospace Engineering

LOW ORDER RECONSTRUCTION AND MODELING OF SUPERSONIC PARACHUTE UNSTEADY AERODYNAMICS

Thesis advisor: Prof. Francesco Picano
Thesis co-advisor: Ing. Luca Placco

Candidate: Samuele Nizzardo
Matriculation number: 2004152

Academic year 2021-2022

To my dad Bruno and my nephew Isacco

Abstract

The main objective of this master thesis project is to apply Proper Orthogonal Decomposition (POD) to the results obtained from a Large-Eddy Simulation of a rigid supersonic parachute trailing behind a descent module as it travels through the atmosphere of Mars. The most important goal is to obtain an accurate reconstruction of the original dynamics using the least amount of modes that compose the flow field. This will preserve the entire time- evolving nature and behaviour of the system while filtering and reducing the amount of data required to represent the whole phenomenon. We observe that ten flow modes are enough to achieve this target. The results obtained are examined in terms of instantaneous and mean fields. The reconstruction of instantaneous fields reveals the presence of canonical flow regions around the parachute, like normal shock and the turbulent wake. In particular, specific attention is given to the interaction between the turbulent wake produced by the capsule and the bow shock ahead of the parachute; fluctuations of the wake are amplified as they cross the shock, leading to strong flow oscillations and potential system instability, due to the so called parachute 'breathing' cycle. The comparison of the POD results was performed both by evaluating the instantaneous two dimensional fields and one-dimensional profiles of the reconstructed flow and also by addressing the root-mean-square fluctuations associated to the results averaged in time. The ultimate intention related to the performed research activity was to show how POD data analysis proves to be an excellent candidate to provide a low order reconstruction of flow unsteadiness. The results obtained can be potentially implemented in static aerodynamic databases to aid in the description of the flight instabilities related to parachute oscillations that contribute to the deviation from the nominal reentry trajectory.

Contents

List of Figures

1 | Introduction

Since their discovery, Navier-Stokes equations cannot be analytically solved and this causes the necessity of using iterative methods. The problem of those methods dwells essentially in the these two issues:

- we get the almost exact solution[1] (for instance, with DNS [20]), but with a huge computational cost;
- we obtain a less accurate solution (e.g. with RANS [15]), instead requires a reasonable computational time.

In particular, turbulence flows involve the interaction of many degrees of freedom over broad ranges of spatial and temporal scales [5], so the intricacy of the problem increases further. At the present day, many computational methods that deal with turbulence flows (e.g. wall modeled large eddy simulation, modal analysis methods, etc.) were developed by researchers, but this is still a strongly developing sector.
The motivation of this thesis work lies in the recent failure of the ESA's ExoMars 2016 mission. We will provide more details regarding the ESA's ExoMars mission in the first section, together with its specifics, evaluating also the related problem of *breathing cycle* connected to the parachute device. Modal analysis techniques and Proper orthogonal decomposition will be then presented.

1.1 ESA's ExoMars mission

ExoMars program consists of two mission:

1. the deliver of Trace Gas Orbiter (TGO)[2] and Schiaparelli EDL demonstrator,[3] launched in 2016;

[1] *Almost exact solution* just because there is the necessity to iterate to obtain the solution (which is not exact); this is due to the fact that, as already said, there is no analytical solution.

[2] TGO is an orbiter launched to investigate on subsurface water and atmospheric trace gases with the goal to acquire information on possible on-going biological or hydrothermal processes.[28]

[3] EDL is an European Entry, Descent, and Landing demonstrator equipped to perform measurements during descent and on the martian surface.[28]

2. the launch of two science elements to the martian surface, which are *Kazachock* -a surface platform instrumented to perform environmental and geophysics measurements- and *Rosalind Franklin* -a rover tasked with conducting a search for signs of life.-
   To date, owed to the suspension of collaboration with Russian space agency, this second part of the mission might be delivered to 2028.

1.1.1 ExoMars 2016

The ExoMars 2016 mission was launched on March 2016 and after six months of interplanetary cruise, TGO delivered Schiaparelli toward Mars. On October 2016, Schiaparelli flew in the Mars atmosphere and after a successful entry, it failed the last part of the descent, crashing on Mars ground [1]. A hypersonic entry should have been followed by a passive parachute descent and an active proximity phase: thanks to the activation of retrorockets, horizontal accuracy of the landing would have been improved. Schiaparelli would have finally landed on a crushable structure, designed to soften the impact [13].

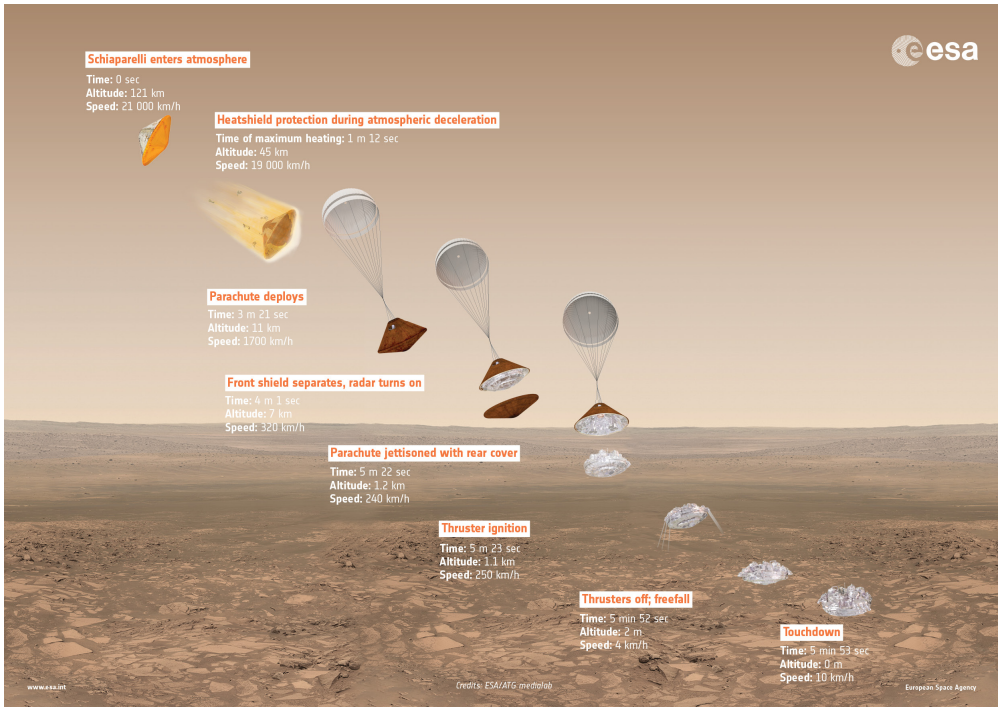

Figure 1.1: Representation of the EDL sequence of ESA's ExoMars 2016 mission [1].

However, the capsule began to oscillate with an angular rates that exceeded the saturation limit of the Inertial Measurement Unit (IMU), immediately after the parachute inflation; so, the sensor saturated, providing to the control software the wrong attitude of the module. This caused an incorrect altitude calculation and a premature activation of the final descent phase. Hence, Schiaparelli impacted the surface at a speed over the $300\,km/h$. Schiaparelli Anomaly Inquire report [27] attributes the main cause of the failure to the coupling of the large parachute motion (due to the unsteady wake dynamics) and the force oscillation on the

riser (owed to the parachute area variation) because they were not sufficiently studied during the design phases.

1.1.2 Rosalind Franklin (former ExoMars 2022)

ESA's ExoMars 2022 mission foresaw the departure at the end of September 2022, with an arrival on June 2023. The spacecraft composite was to consist of a carrier module (CM) and a descent module (DM) [28]:

- CM must execute all maneuvers during the interplanetary transfer and release the DM for landing on Mars;
- DM had to decelerate due to the atmospheric frictional drag and then, a guidance navigation and control algorithm had to trigger the opening of the first supersonic parachute. A second subsonic canopy had to be deployed around 540 km/h and at 2 km of altitude the DM had to start to monitor the distance to the ground and the vertical/horizontal velocity vector, in order to perform the soil relative navigation. At 1 km above the surface, the lander had to detach from back shell and parachute, going into a free-fall. In the end, the lander had to decelerate by using the main engines, obtaining a dampen touch down.

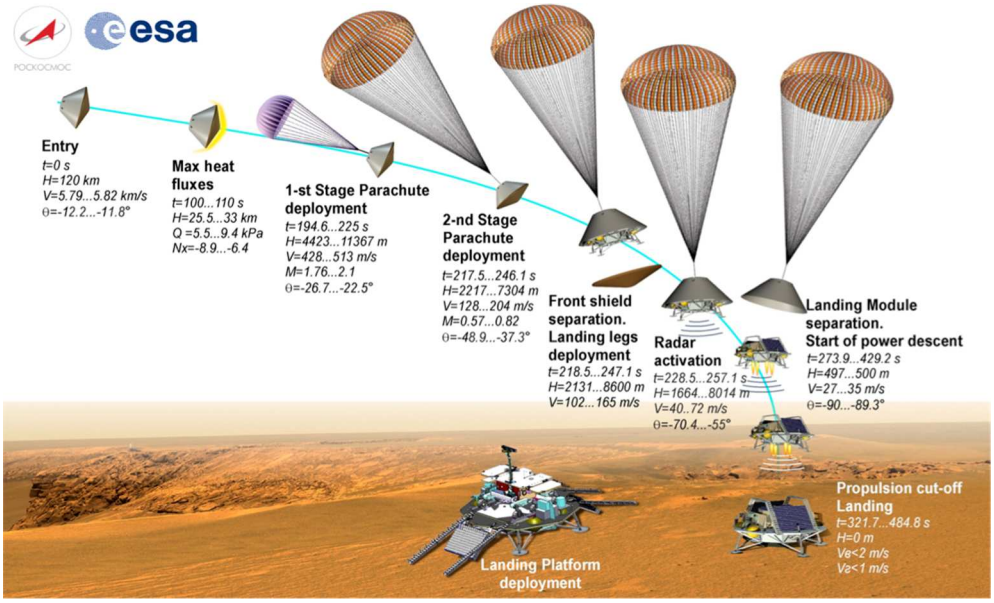

Figure 1.2: Representation of the EDL sequence of ESA's ExoMars 2022 mission.

Because of the current developments in the geopolitical situation[4], the launch scheduled for 2022 has been aborted and the new take-off is planned for 2028, with the new mission name of Rosalind Franklin.

[4]ExoMars mission had to be an international project between ESA and Roscosmos, the Russian space agency.

1.2 Supersonic parachute

Supersonic decelerators are widely used for planetary mission during entry and descent phases, into the low-density atmospheres (e.g. Martian atmosphere). They are considered as the most critical element in designing the EDL phase as they provide proper control of altitude and descent velocity during the descent through the planet atmosphere. Canopies are designed to be very light and have an high packaging efficiency; this allow parachutes to be very efficient in their mass/volume ratio, proving to be invaluable when employed as aerodynamic decelerators [10] [31]. The performances of supersonic parachute in terms of velocity and altitude (that means in term of density) may be shown in figure 1.3:

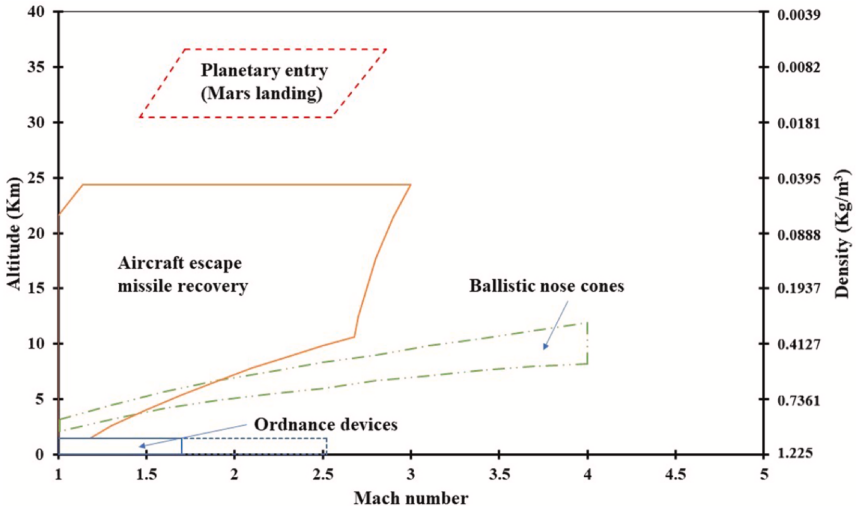

Figure 1.3: Supersonic parachute performances [31].

The parachute used in this thesis is quite similar to a Disk-Gap-Band (DGB) canopy, but without the ”band” (for further details, see section 2.5). In the earliest studies of parachutes, researchers tried to put a conventional canopy in a supersonic flow: when a parachute is placed in a supersonic flow, the capsule wake interacts with the parachute shock-wave (coupled with the structural dynamics of the flexible canopy), causing not negligible pressure fluctuations in the parachute. Those pressure oscillations origin some large canopy deformations, including the breathing cycle oscillation (see next section 1.2.1), above Mach 1.5: the consequence is the relative low and unstable drag coefficient, which might causes a critical damage of the parachute [24]. This is why DGB canopy (shown in figure 1.4 with capsule and wires) is the only one which may be used in the supersonic conditions. Stability and drag coefficient are the principal criteria used to define the performance of a parachute: drag increases when Mach number grows from 1.2 to 1.8 or from 1.8 to 2.0, but it decreases for higher Mach number. In particular, the coupling between capsule wake and canopy shock, origins drag losses and with the increasing of Mach number, breathing phenomena, fabric dynamics and dynamic loads increase [31].

The stability of a supersonic parachute is an important goal to achieve in order to get the best behavior of the canopy and, as consequence, the stability of the capsule; this stability,

which may be static or dynamic, considers many parameters, such as canopy configuration, parachute distance by the capsule and the interactions between capsule wake and canopy shock. Stability can be improved by increasing the geometric porosity (e.g. changing the vent diameter), increasing the fabric permeability, the parachute radius and the band height (etc.) [7]. However, a compromise is necessary because as the porosity increases, we observe a decrease in the drag coefficient: indeed, drag coefficient is affected by the total porosity and a parachute with a lower total porosity has a higher drag coefficient [8].

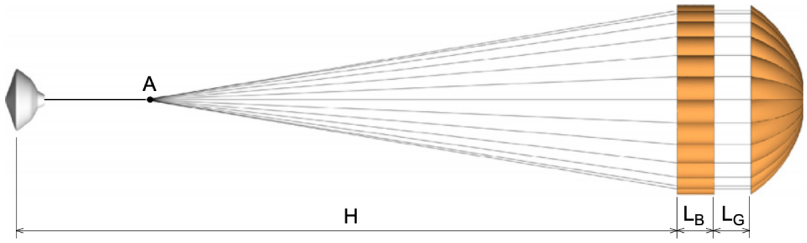

Figure 1.4: DGB parachute configuration, represented with capsule and wires [17].

1.2.1 Breathing cycle

We define as *breathing cycle* the periodic inflation and deflation motion of the parachute canopy when subjected to a supersonic unsteady turbulent flow. This phenomenon is owed to the cyclical variation of suction pressure, resulting from the passage of vortex structures, around the exterior surface of the canopy [16], as shown in figure 1.5.

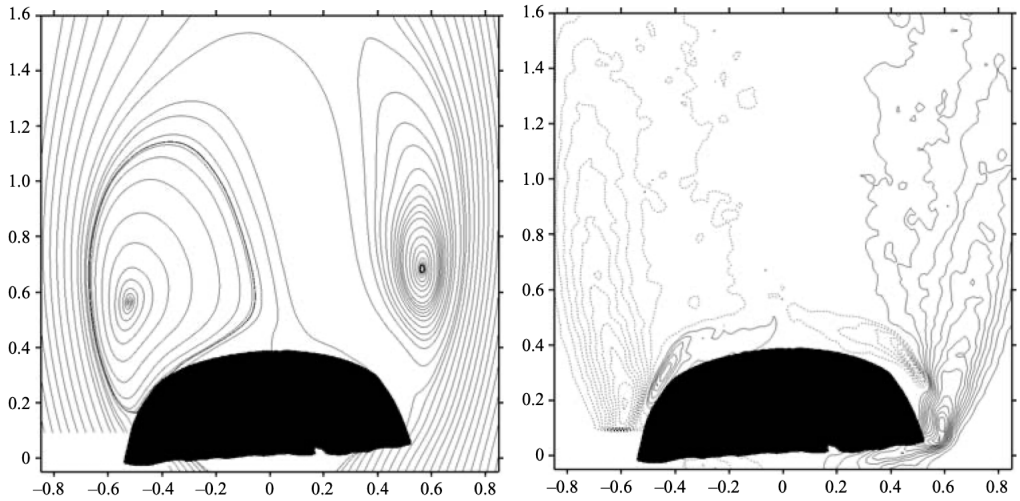

(a) Time-averaged streamlines

(b) Vorticity contours at $Re \approx 3.0 \cdot 10^4$

Figure 1.5: Vortexes on the parachute which cause the breathing cycle. X-axis represent the dimensionless radial velocity r/D_p (where D_p is the canopy diameter), while Y-axis represents the non-dimensional coordinate z/D_p [16].

The parachute shock is perturbed by the unstationary phenomena of the capsule wake and the fluctuations of pressure (and also of the momentum) become stronger as they pass

through the shock-wave. These changes cause large deformations in the inflated shape of the parachute and bow shock (that is the canopy shock) oscillations, which further bolster the unsteadiness of the pressure in the canopy. A noticeable detail is that is not required a flexible parachute to generate the irregular dynamics of the canopy shock [3] [17]. In the following figure is shown a typical trend of the breathing cycle:

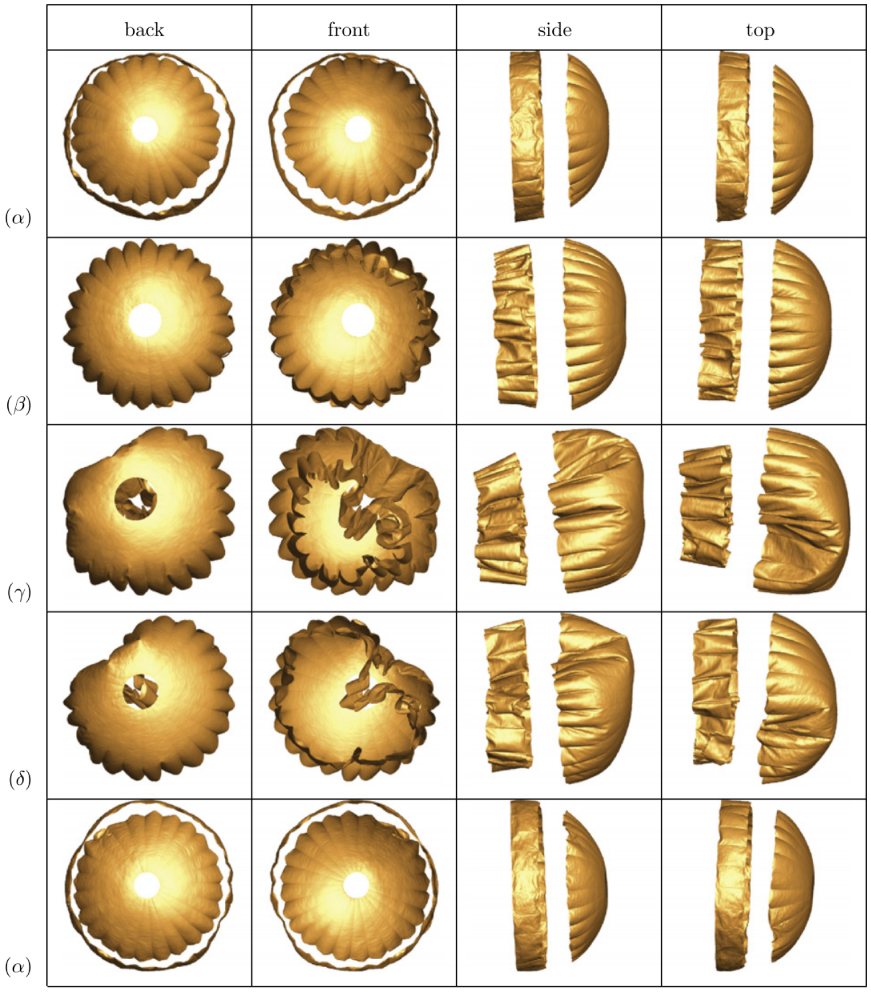

Figure 1.6: DGB parachute: phases of breathing cycle [17].

In figure 1.6, (α) corresponds to maximum inflation point, (β) is the average inflation, (γ) represents the minimum inflation, while (δ) is again the average inflation, but before that parachute reverts to the maximum inflation.

1.3 Modal decomposition

In recent years there has been an increased interest in model reduction which uses modal decomposition techniques to analyze the underlying dynamics connected to extended flow field data. The success/advantage connected to these methods resides in the ability to decompose the complex unsteady flow-field into several flow independent elements. These, taken sepa-

rately, can aid in the analysis of the dynamics and highlight different flow properties. Proper Orthogonal Decomposition (POD) is the most widely used method: it categorizes modes by their relative energy content, separating them from their temporal dependency [19].
As highlighted in [26], there are strengths and weaknesses of POD.
Strengths:

- It provides an orthogonal set of basis vectors with the minimal dimension. This property is useful in constructing a reduced-order model of the flowfield.
- POD modes are simple to compute; notably, the snapshots POD method is mainly attractive for high-dimensional spatial datasets.
- Data incoherent noise generally appears at high-order of energy modes, provided that the noise level is lower than the signal level. POD analysis may be used to remove that disturb from the dataset by removing high-order modes, as is generally done.
- POD analysis is extensively used in a wide spectrum of studies.

Weaknesses:

- Since POD is based on second-order correlation, higher-order correlations are left out.
- Temporal coefficients of spatial POD modes generally contain a mix of frequencies: a single mode cannot identify a specific energy content.
- POD modes are not dynamically arranged, but are sorted from the most energetic mode to the least one.

2 | Methodology

In this chapter we explain theory and methods behind Proper Orthogonal Decomposition and Large Eddy Simulation (hints), starting by balance equations. Then we show the numerical method used, exhibit the simulation setup and explain the POD method.

2.1 Balance equations

The mathematical model [2] [25] describing the problem is based on the Navier-Stokes equations, which express the balance for a Newtonian, isotropic fluid. These equations are derived from three fundamental principles of physics:

1. mass conservation;
2. momentum conservation;
3. energy conservation.

In particular, Navier-Stokes equations consist of the momentum equations only, but as it often happens for convenience, we call Navier-Stokes equations the entire system made by mass, momentum and energy conservation equations.
For a compressible, viscous and heat-conducting gas (neglecting heat exchanged by radiation), we can write Navier-Stokes equations using index notation as:

$$\frac{\partial \rho}{\partial t} + \frac{\partial (\rho u_j)}{\partial x_j} = 0 \tag{2.1}$$

$$\frac{\partial (\rho u_i)}{\partial t} + \frac{\partial (\rho u_i u_j)}{\partial x_j} + \frac{\partial p}{\partial x_j} - \frac{\partial \sigma_{ij}}{\partial x_j} = 0 \tag{2.2}$$

$$\frac{\partial (\rho e)}{\partial t} + \frac{\partial (\rho e u_j + p u_j)}{\partial x_j} + \frac{\partial q_j}{\partial x_j} - \frac{\partial (\sigma_{ij} u_i)}{\partial x_j} = 0 \tag{2.3}$$

where ρ is the gas density, t is the time, x_j is the j-th direction (with $j = 1, 2, 3$), u_j is the velocity component in the j-th direction, p is the thermodynamic pressure, σ_{ij} is the viscous stress tensor, e is the total energy per mass unit and q_j is the total heat flux.
We can express σ_{ij} and q_j as:

$$\sigma_{ij} = \mu \left(\frac{\partial u_i}{\partial x_j} + \frac{\partial u_j}{\partial x_i} - \frac{2}{3} \frac{\partial u_k}{\partial x_k} \delta_{ij} \right) \tag{2.4}$$

$$q_j = \lambda \frac{\partial T}{\partial x_j} \tag{2.5}$$

where μ is the gas dynamic viscosity, δ_{ij} is the Kronecker delta, λ is the heat transfer coefficient, and T is the gas temperature.
This model consists of 5 equations with 7 unknowns, which are ρ, u_j, p, e and T: we need to add some equations in order to complete the system and we can do that using the following equations. In particular, we assume the gas as an ideal gas, so we use a state equation and a constitutive equation for total energy:

$$p = \rho R T \tag{2.6}$$

$$e = c_v T + \frac{u_i u_i}{2} \tag{2.7}$$

where R is the specific gas constant (which is defined as $R = \mathscr{R}/\mathscr{M}$, with $\mathscr{R} = 8.314\,\mathrm{J\,mol^{-1}\,K^{-1}}$ universal gas constant, and $\mathscr{M}$ $[\mathrm{kg\,mol^{-1}}]$ molar mass of the gas) and c_v is the heat coefficient at constant volume.
Navier-Stokes equations is now self sustained. We can re-write these equations in a non-dimensional form, so that known dimensionless groups can be introduced.

2.1.1 Non-dimensional Navier-Stokes equations

The adimensional form of Navier-Stokes equations is useful to minimize the number of independent parameters which control the system, as well as normalize the relevant quantities to be order one, thus reducing the computational cost. Non-dimensional quantities (indicated with the superscript ') are obtained through a change of variables: each dimensional variable is expressed as the product between the corresponding dimensionless variable and a reference quantity (which is indicated with the subscript *0*). So we have the following adimensional values:

$$\begin{aligned} x' &= \frac{x}{l_0} \quad , \quad u_i' = \frac{u_i}{u_0} \quad , \quad \rho' = \frac{\rho}{\rho_0} \quad , \quad t' = \frac{t}{t_0} \\ e' &= \frac{e}{e_0} \quad , \quad T' = \frac{T}{T_0} \quad , \quad \mu' = \frac{\mu}{\mu_0} \quad , \quad \lambda' = \frac{\lambda}{\lambda_0} \end{aligned} \tag{2.8}$$

Reference values are arbitrary and we have defined them as:

$$\begin{cases} \rho_0 = \rho_\infty \\ p_0 = p_\infty \\ T_0 = T_\infty \\ l_0 = D_0 \end{cases} \quad \Longrightarrow \quad \begin{cases} R_0 = \frac{p_0}{\rho_0 T_0} \\ u_0 = \sqrt{R_0 T_0} \\ t_0 = \frac{l_0}{u_0} \\ \mu_0 = \rho_0 u_0 l_0 \\ \lambda_0 = \mu_0 R_0 \\ c_{p0} = \frac{\gamma R_0}{\gamma - 1} \\ c_{v0} = \frac{R_0}{\gamma - 1} \\ e_0 = c_{v0} T_0 + \frac{u_0^2}{2} \end{cases} \tag{2.9}$$

where c_p is the heat coefficient at constant pressure, c_v is the heat coefficient at constant volume, l_0 is the reference length (set equal to the parachute diameter $D_0 = 2R_0$) and γ is the specific heat ratio. With this choice we obtain unitary free-stream quantities:

$$\rho'_\infty = p'_\infty = T'_\infty = R'_\infty = 1$$

We can now introduce 4 fundamental non-dimensional groups using the Buckingham's theorem (also said Π thoerem), starting from reference values of 2.9:

$$\begin{array}{lcccl}
\text{Specific heat ratio} & \longleftrightarrow & \dfrac{\text{Enthalpy}}{\text{Internal energy}} & \longleftrightarrow & \gamma = \dfrac{c_{p0}}{c_{v0}} \\
\text{Mach number} & \longleftrightarrow & \dfrac{\text{Velocity}}{\text{Speed of sound}} & \longleftrightarrow & M_\infty = \dfrac{u_\infty}{a_\infty} \\
\text{Reynolds number} & \longleftrightarrow & \dfrac{\text{Inertial forces}}{\text{Viscous forces}} & \longleftrightarrow & Re = \dfrac{\rho_0 l_0 u_\infty}{\mu_\infty} \\
\text{Prandtl number} & \longleftrightarrow & \dfrac{\text{Viscous diffusion}}{\text{Thermal diffusion}} & \longleftrightarrow & Pr = c_{p0}\dfrac{\mu_\infty}{\lambda_\infty}
\end{array}$$

where the free-stream speed of sound a_∞ can be expressed as:

$$a_\infty = \sqrt{\gamma R_0 T_0} \tag{2.10}$$

From these groups we can now compute the non-dimensional free-stream quantities of the velocity (u'_∞), gas dynamic viscosity (μ'_∞) and heat transfer coefficient (λ'_∞). As we did in 2.8, we normalize those values and obtain:

$$u'_\infty = \frac{u_\infty}{u_0} = \frac{M_\infty a_\infty}{\sqrt{R_0 T_0}} = \sqrt{\gamma} M_\infty \tag{2.11}$$

$$\mu'_\infty = \frac{\mu_\infty}{\mu_0} = \frac{\rho_0 l_0 u_\infty}{Re} \cdot \frac{1}{\rho_0 l_0 u_0} = \frac{\sqrt{\gamma} M_\infty}{Re} = \frac{u'_\infty}{Re} \tag{2.12}$$

$$\lambda'_\infty = \frac{\lambda_\infty}{\lambda_0} = \mu_\infty \frac{c_{p0}}{Pr} \cdot \frac{1}{\rho_0 l_0 u_0 R_0} = \frac{\gamma}{\gamma - 1} \cdot \frac{1}{Pr} \cdot \frac{\sqrt{\gamma} M_\infty}{Re} = \frac{\gamma}{\gamma - 1} \cdot \frac{\mu'_\infty}{Pr} \tag{2.13}$$

In order to be clearer, we now use non-dimensional quantity only, omitting the superscript used so far. It is now possible re-write the Navier-Stokes equations in the dimensionless form:

$$\frac{\partial \rho}{\partial t} + \frac{\partial (\rho u_j)}{\partial x_j} = 0 \tag{2.14}$$

$$\frac{\partial (\rho u_i)}{\partial t} + \frac{\partial (\rho u_i u_j)}{\partial x_j} + \frac{\partial p}{\partial x_j} - \frac{\sqrt{\gamma} M_\infty}{Re} \cdot \frac{\partial \sigma_{ij}}{\partial x_j} = 0 \tag{2.15}$$

$$\frac{\partial (\rho e)}{\partial t} + \frac{\partial (\rho e u_j + p u_j)}{\partial x_j} - \frac{\sqrt{\gamma} M_\infty}{Re} \left[\frac{\partial (\sigma_{ij} u_i)}{\partial x_j} - \frac{\gamma}{\gamma - 1} \cdot \frac{1}{Pr} \cdot \frac{\partial q_j}{\partial x_j} \right] = 0 \tag{2.16}$$

Prandtl number and heat specific ratio are considered constant, using the hypothesis of calorically perfect gas - it is possible to use this one until the temperature is lower than 1000 K; in this case, the maximum temperature of the gas is about 400 K.
Simulation and reconstruction parameters were set to replicate the Martian atmosphere,

considering CO_2 as a perfect gas, hence we utilize the following parameters:

$$\gamma = 1.30 \quad , \quad Pr = 0.72 \quad , \quad M_\infty = 2 \quad , \quad Re = 10^6$$

We have chosen this value of free-stream Mach number because it corresponds to the parachute deployment Mach number (that is a critical stage of the re-entry maneuver). From these values, non-dimensional free-stream velocity and viscosity can be easily calculated in this way:

$$u_\infty = \sqrt{\gamma} M_\infty \approx 2.28 \tag{2.17}$$

$$\mu_\infty = \frac{u_\infty}{Re} \approx 2.28 \cdot 10^{-6} \tag{2.18}$$

Dynamic viscosity and heat transfer coefficient both depend on the gas temperature, so that they are expressed as (all quantities are normalized by their reference values):

$$\mu = \mu(T) = \mu_\infty T^{0.76} \tag{2.19}$$

$$\lambda = \lambda(T) = \frac{\gamma}{\gamma - 1} \cdot \frac{\mu}{Pr} \approx 1.37 \cdot 10^{-5}\, T^{0.76} \tag{2.20}$$

We assume that viscosity follows the Power-law of a generalized flow: we decide not to use the Sutherland's law because its constant is not calibrated for the Martian atmosphere.

2.2 Turbulent regime scales

In this section we briefly explain the energy cascade theory and the Richardson and Kolmogorov model (also said *K41* model), then we understand the phenomenon which characterizes the eddy viscosity.

The energy cascade concept consists of transferring the energy content of large vortex structures to smaller ones, until the phenomenon reaches sufficiently small scales, such that the viscosity becomes relevant in order that energy can be dissipated. For $Re >> 1$, is known that viscosity is negligible at larger scales, but in the smaller scales (known as *universal scales*), - where vortexes are ever smaller - local gradients grow increasingly and so, viscosity get a dominant role.
It is possible to subdivide the energy cascade region in 3 macro areas:

1. big scales, also known as l_0 *scale*;

2. mid scales, or *inertial range*;

3. small scales, known as *Kolmogorov microscale* or *K41* model.

2.2.1 l_0 SCALE

This scale is the biggest one, where there are the largest vortrex structure with the major quantity of energy. The requirements to be defined as l_0 scale are these:

$$l_0 \simeq L_0 \quad , \quad u_{l_0} \simeq u'_{rms} = \sqrt{\frac{2}{3}k} \tag{2.21}$$

where l_0 is the characteristic dimension of the biggest vortex, L_0 is the characteristic dimension of the case, u_{l_0} is the characteristic velocity of the biggest vortex, u'_{rms} is the root mean square value of the fluctuating velocity - it is experimentally found that $u'_{rms} \approx (0.1 \div 0.3)U_0$ -, U_0 is the undisturbed flow velocity and k is the turbulent kinetic energy.
It is possible to define the Reynolds number for the big scales as Re_{l_0}:

$$Re_{l_0} = \frac{u_{l_0} l_0}{\nu} \simeq \frac{u'_{rms} l_0}{\nu} \simeq \frac{U_0 L_0}{\nu} = Re \tag{2.22}$$

where ν is the cinematic viscosity ($\nu = \rho/\mu$).
Another fundamental concept to consider is how much energy can be transfer from the big scale, to the smaller one. Considering $l_0 = L_0$ and calling τ_{l_0} as the characteristic life time (i.e. the time during which energy exchange occurs), the turbulent kinetic energy introduced per time unit is proportional to:

$$\frac{k_{l_0}}{\tau_{l_0}} \simeq \frac{u_{l_0}^3}{l_0} \simeq \frac{U_0^3}{L_0} \tag{2.23}$$

2.2.2 KOLMOGOROV MICROSCALE

Kolmogorov microscale consist of the dissipative range, where the dimension l of this region is proportional to the smallest vortex dimensions η; in particular:

$$l \simeq \eta \ll l_0$$

At this scale, the behavior of the vortex structures becomes *universal*, - which means vortexes are not affected by the main flow (so neither from geometry) - thus flow turn to isotropic and homogeneous.
In the K41 model, the following two hypotheses apply:

Hypothesis 0: if $Re \gg 1$ and $l \ll l_0$, then flow is locally isotropic and homogeneous, statistics of these scales are universal and they depend at best on ν and ε (that is the *dissipation* term of turbulent energy equation);

I similarity hypothesis: smallest scales depend on ν and ε only.

With this knowledge, we can define characteristic dimension, velocity and time of Kolmogorov scale respectively as:

$$\eta = \left(\frac{\nu^3}{\varepsilon}\right)^{\frac{1}{4}} \quad , \quad u_\eta = (\nu\,\eta)^{\frac{1}{4}} \quad , \quad \tau_\eta = \frac{\eta}{\tau_\eta} = \left(\frac{\nu}{\varepsilon}\right)^{\frac{1}{2}} \tag{2.24}$$

Considering these relations, we can also define the Reynolds number and the dissipation as:

$$Re_\eta = \frac{u_\eta \eta}{\nu} = \frac{\nu}{\nu} = 1 \quad , \quad \varepsilon_\eta \simeq \nu\left(\frac{u_\eta}{\eta}\right)^2 = \frac{\nu^{\frac{3}{2}}}{\nu^{\frac{3}{2}}}\varepsilon^1 = \varepsilon \tag{2.25}$$

So, it is clear that kinematic viscosity ν plays a key role at these scales, thus dissipation due to Kolmogorov scales ε_η is approximately equal to the turbulent flow dissipation ε.

2.2.3 Inertial range

The inertial range (also known as Taylor microscale) is the scale between l_0 and Kolmogorov scales, where the characteristic length l is:

$$\eta \ll l \ll l_0$$

Also for this mid scale, we need to add a hypothesis:

II similarity hypothesis: if $Re \gg 1$ and $\eta \ll l \ll l_0$, statistics are universal, but independent by the kinematic viscosity ν; hence, there is only turbulent flow dissipation ϵ dependence (and implicitly by l).

This dissipation is not a real term of "consumption" of energy because, as said before, at these scales there is the energy transfer to the smallest vortex structures.
Therefore, characteristic velocity of these structures is:

$$u_l = (\varepsilon\, l)^{\frac{1}{3}} \tag{2.26}$$

To confirm the second similarity hypothesis we have to verify that the Reynolds number of inertial range $Re_l \gg 1$; thus:

$$Re_l = \frac{u_l\, l}{\nu} = \left(\frac{l}{\eta}\right)^{\frac{4}{3}} \quad \Longrightarrow \quad Re_l \gg 1 \tag{2.27}$$

Again, the transferred energy from big scales to smallest ones ε_l is:

$$\varepsilon_l \simeq \frac{k_l}{\tau_l} \simeq \frac{u_l^2}{\frac{l}{u_l}} = \varepsilon\,\frac{l}{l} = \varepsilon \tag{2.28}$$

where k_l is the turbulent kinetic energy and τ_l is the time of the scale.

After this brief explanation of the energy cascade theory, we show it in the following picture:

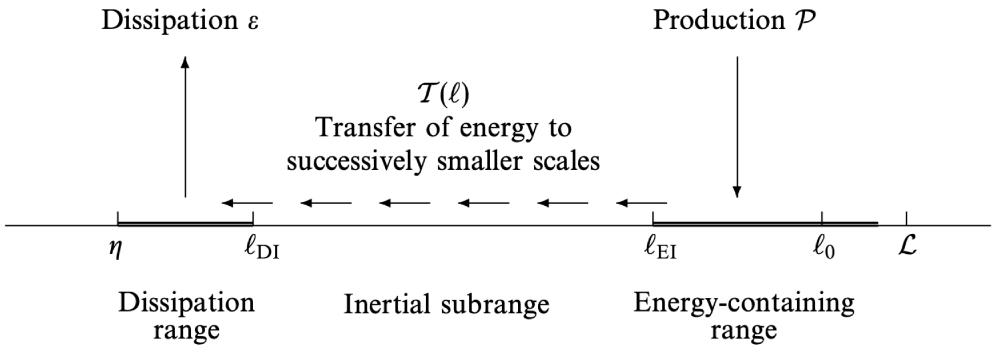

Figure 2.1: Energy cascade [21].

Production $\mathscr{P}$ is the term that dissipates the energy from mean field K to feed turbulent filed k, which in turn is dissipated through the dissipation term ε. The understanding of the energy cascade mechanism will be fundamental for introducing the different computational techniques.

2.3 Numerical method

We present the three main computational strategies for solving Navier-Stokes equations. In the next paragraphs we understand the difference between these three methods and why LES can be considered the current state of art in computational fluid dynamics.

2.3.1 Direct Numerical Simulation

DNS solves Navier-Stokes equations in order to get an instantaneous field as result. This technique is extremely accurate, but costly too because the simulation requires the solution of the whole energy cascade process. In fact, grid-step Δ is of the same order of magnitude of the Kolmogorov's vortexes:

$$\Delta \simeq \eta$$

Another feature of DNS is that the characteristic length is similar to the domain dimension, in fact:

$$L_x \simeq L_y \simeq L_z \simeq L_0$$

The problem of this simulation is the computational time, because the total number of points N_{DNS} required for obtaining a converging solution is very high:

$$N_{DNS} \simeq Re^{\frac{9}{4}} \quad \Longrightarrow \quad N_{\Delta t} = \frac{T}{\Delta t} \simeq \frac{T_0}{\tau_\eta} \propto Re^{\frac{1}{2}}$$

where:

- $N_{\Delta t}$ are the time instants to be simulated;
- T is the simulation time;

- T_0 is the big scales time;
- Δt is the time-step;
- τ_η is the Kolmogorov microscales time.

It is clear that, to date, DNS can only be used for the simplest cases.

2.3.2 Reynolds Averaged Navier-Stokes

Reynolds Averaged Navier-Stokes is a flow simulation technique that consists of solving the time-averaged Navier-Stokes equations; these equations need a turbulence closing model because of the presence of the Reynolds Stress tensor. RANS represents the standard of industry simulation given the low computational cost connected, but it provides mean fields only and turbulence modeling requires particular attention.
Before analyzing RANS, we have to introduce the Reynolds average operation (also said time-averaging). Taking velocity as reference (just for simplicity's sake), this average consists of:

$$\overline{u(x,t)} = U(x,t) = \frac{1}{N}\sum_{k=1}^{N} u^{(k)}(x,t) \tag{2.29}$$

where N is the experiment number ($N \gg 1$), $u^{(k)}(x,t)$ is the measured velocity of each experiment and $U(x,t)$ is the Reynolds-averaged velocity.
It is possible to decompose instantaneous velocity $u(x,t)$ in two terms: the Reynolds-averaged velocity $U(x,t)$ and $u'(x,t)$, that is the velocity fluctuations term; hence:

$$u(x,t) = U(x,t) + u'(x,t) \tag{2.30}$$

For all this section, capital letters refer to the time-averaged quantities, while terms with superscript ['] refer to fluctuating quantities. For compressible, the density weighted Favre averaging (indicated by [$\tilde{.}$])

$$\tilde{u}_i = \frac{\overline{\rho u_i}}{\bar{\rho}} \tag{2.31}$$

is a more useful concept than the traditional Reynolds averaging (note that $\overline{\rho u_i}$ is the Reynolds-averaging of (ρu_i) and $\bar{\rho}$ is the Reynolds-averaged density). Nevertheless, RANS equations are written using the traditional Reynolds-averaging concept instead of the Favre averaging, although the mean-flow solution method used is suitable for compressible flows. So, dimensionless RANS for incompressible flow may be written as [15]:

$$\frac{\partial U_i}{\partial x_i} = 0 \tag{2.32}$$

$$\frac{\partial U_i}{\partial t} + U_j\frac{\partial U_i}{\partial x_j} + \frac{1}{\rho}\frac{\partial P}{\partial x_i} - \frac{\partial}{\partial x_j}\left(\nu\frac{\partial U_i}{\partial x_j}\right) + \frac{\partial\left(\overline{u_i'u_j'}\right)}{\partial x_j} = 0 \tag{2.33}$$

The only difference between RANS and Navier-Stokes equations is the last term, which is the divergence of $\overline{u_i'u_j'}$: this is known as *Reynolds stress tensor* and it tends to even out the

flow (opposing the gradient $\partial U_i/\partial x_j$). That term is a second order symmetric tensor, but it depends on a three-fold correlation - that problem persists even if the initial equation order raise up and it called *closure problem*:

$$\frac{\mathbf{D}(\overline{u_i' u_j'})}{\mathbf{D}t} = \mathscr{F}(\overline{u_i' u_j' u_k'})$$

where $\frac{\mathbf{D}}{\mathbf{D}t}$ is the material derivative[1] and $\mathscr{F}$ is a generic function.
This issue for the Reynolds stress tensor can be solved using an energy transport equation, so it is:

$$\frac{\mathbf{D}(\overline{u_i' u_j'})}{\mathbf{D}t} = \mathcal{P}_{ij} - \varepsilon_{ij} + \Phi_{ij} + \mathcal{D}_{ij} \tag{2.34}$$

where:

- $\mathcal{P}_{ij} = -\overline{u_j' u_k'}\frac{\partial U_i}{\partial x_k} - \overline{u_i' u_k'}\frac{\partial U_j}{\partial x_k}$ $\longrightarrow$ $\mathcal{P}_{ij} = \textit{Production}$
- $\varepsilon_{ij} = 2\nu\overline{\frac{\partial u_i'}{\partial x_k}\frac{\partial u_j'}{\partial x_k}}$ $\longrightarrow$ $\varepsilon_{ij} = \textit{Dissipation}$
- $\Phi_{ij} = \frac{1}{\rho}\overline{p'\left(\frac{\partial u_i'}{\partial x_j} + \frac{\partial u_j'}{\partial x_i}\right)}$ $\longrightarrow$ $\Phi_{ij} = \textit{Redistribution}$
- $\mathcal{D}_{ij} = \frac{\partial}{\partial x_k}\left(-\overline{u_i' u_j' u_k'} - \frac{1}{\rho}\left(\delta_{ik}\overline{p' u_j'} + \delta_{jk}\overline{p' u_i'}\right) + \nu\frac{\partial\overline{u_i' u_j'}}{\partial x_k}\right)$ $\longrightarrow$ $\mathcal{D}_{ij} = \textit{Fluxes}$

$\mathcal{P}_{ij}$ is the rate at which energy is fed from the mean flow to each stress component, ε_{ij} is a viscous dissipative term which cannot be computed from available variables (hence it must be modeled), Φ_{ij} is the redistribution term, because its trace is zero and thus it neither introduces nor subtract mechanical energy and, in the end, $\mathcal{D}_{ij}$ is the sum of three fluxes (*i.e.* the transport by velocity fluctuations, the pressure transport flux, and the viscous flux of each stress component).
Equation 2.34 explains the behavior of the aforementioned energy cascade (section 2.2), starting from the largest vortexes to the dissipation range, passing through the inertial range.
To solve RANS equations, it is necessary to use a turbulence model. There are a lot of them, as $k-\varepsilon$ model, $k-\omega$ model (both based on Boussinesq hypothesis[2]), *Menter* model, Spalart-Allmaras model and so on. Just to understand how a turbulence model is made, we very briefly describe the $k-\varepsilon$ model [21].

The $k-\varepsilon$ model belongs to the class of two-equation models, in which model transport equations are solved for two turbulence quantities (the turbulent kinetic energy k and the viscous dissipation ε). From these quantities, reference values may be calculated such a length-scale ($L = k^{3/2}/\varepsilon$), a time-scale ($\tau = k/\varepsilon$), etc. In addition to the Boussinesq hypothesis, this model consists of:

1. a model transport equation for k;

[1] Material derivative is defined as $\frac{\mathbf{D}U_i}{\mathbf{D}t} = \frac{\partial U_i}{\partial t} + U_j\frac{\partial U_i}{\partial x_j}$

[2] Boussinesq hypothesis introduces a turbulence viscosity ν_t and it defines Reynolds stress tensor and molecular stress tensor as similar.

2. a model transport equation for ε;

3. the explanation of the turbulent viscosity as $\nu_t = C_\mu \frac{k^2}{\varepsilon}$.

$C_\mu = 0.09$ is one of the five calibration constants of the model; these five constants are arbitrary and properly tuned according to the type of flow analyzed.

2.3.3 Large Eddy Simulation

Large Eddy Simulation (or simply LES) is a flow simulation technique which allows to solve unstationary cases: it solves large vortex structures, while filtering and smothering the smaller ones (only the universal scales).
To obtain LES, we introduce a low-pass filter to the Navier-Stokes equations. Filtering is done by decomposing a generic variable (e.g. X-direction velocity u) as:

$$u = \bar{u} + u' \tag{2.35}$$

where:

- u is the instantaneous velocity;
- $\bar{u}$ is the filtered velocity and represents the flow field of LES;
- u' is the subgrid velocity; it is composed by high frequencies of the flow, which are the modeled quantities.

The filtering of the equations can be done in explicit (e.g. Top-Hat filter, Gauss filter, etc) or implicit way; in this work, we use an implicit filter, taking advantage of fact that the grid acts as a filter for structures smaller than it. So, we call Δ as grid-step and it is:

$$\Delta = \sqrt[3]{\Delta x\, \Delta y\, \Delta z}$$

It is convenient to express values in terms of density-weighted variables (*Favre* variables) because, in this way, we avoid the appearance of sub-grid terms in the mass balance equation (eq. 2.14) and ensure the filtered governing equations a structurally similar form to the unfiltered one equations. So, a general variable x can be decomposed as:

$$x = \tilde{x} + x'' \tag{2.36}$$

where:

- $\tilde{x} = \frac{\overline{\rho x}}{\bar{\rho}}$ is the density-weighted resolved part;
- x" is the modeled part of x.

Non-dimensional Navier-Stokes equations can be re-written as:

$$\frac{\partial \bar{\rho}}{\partial t} + \frac{\partial(\bar{\rho}\tilde{u}_j)}{\partial x_j} = 0 \tag{2.37}$$

$$\frac{\partial(\bar{\rho}\tilde{u}_i)}{\partial t} + \frac{\partial(\bar{\rho}\tilde{u}_i\tilde{u}_j)}{\partial x_j} + \frac{\partial \bar{p}}{\partial x_j} - \frac{\sqrt{\gamma}M_\infty}{Re} \cdot \frac{\partial \bar{\sigma}_{ij}}{\partial x_j} + \frac{\partial \bar{\tau}_{ij}^{SG}}{\partial x_j} = 0 \tag{2.38}$$

$$\frac{\partial(\bar{\rho}\tilde{e})}{\partial t} + \frac{\partial(\bar{\rho}\tilde{e}\tilde{u}_j + \bar{p}\tilde{u}_j)}{\partial x_j} - \frac{\sqrt{\gamma}M_\infty}{Re}\left[\frac{\partial(\bar{\sigma}_{ij}\tilde{u}_i)}{\partial x_j} - \frac{\gamma}{\gamma-1} \cdot \frac{1}{Pr} \cdot \frac{\partial \tilde{q}_j}{\partial x_j}\right] + \frac{\partial \bar{e}_j^{SG}}{\partial x_j} = 0 \tag{2.39}$$

This is the system after the application of the spatial filter ($\bar{\cdot}$) and the definition of the Favre filter ($\tilde{\cdot}$), known as *dimensionless filtered Navier-Stokes equations*. In particular, the main difference to non-dimensional Navier-Stokes (eq. 2.14, 2.15, 2.16) is the presence of the sub-grid stress tensor ($\bar{\tau}_{ij}^{SG}$) and the sub-grid energy term ($\bar{e}_j^{SG}$), that are:

$$\bar{\tau}_{ij}^{SG} = \bar{\rho}(\overline{u_i u_j} - \tilde{u}_i\tilde{u}_j) \quad , \quad \bar{e}_j^{SG} = \overline{\rho e u_i + p u_i} - (\bar{\rho}\tilde{e}\tilde{u}_i + \bar{p}\tilde{u}_i) \tag{2.40}$$

These two quantities have to be modeled and represent the unresolved turbulent contributions arising from the filtering process. Using the Boussinesq's hypothesis we can assume that turbulence fluctuations act in a dissipative way through a residual viscosity, known as *eddy viscosity* (ν_t). This parameter contains the sub-grid stress tensor and sub-grid energy and it can be modeled as:

$$\nu_t = c_s u_\Delta \Delta \tag{2.41}$$

where:

- $c_s = 0.12 \pm 0.06$ is the Smagorinsky's constant;
- Δ is the grid-step;
- u_Δ is the characteristic velocity on Δ scale.

STREAmS solves the compressible Navier-Stokes equations in dimensionless form (eq. 2.14) without adding any external model, but in order to use this approach we have to discretize Navier-Stokes equation in both space and time. Spatial discretization is based on finite-difference method (see 2.47), but this type of discretization causes a numerical dissipation that can be exploited to achieve an effect similar to eddy viscosity: this is known as *artificial viscosity*. In particular, the discretization of convective terms is characterized by low-pass filters, which provide an implicit sub-grid model naturally coupled to the solvable scales of the flow. So, using this implicit sub-grid model, we can omit conventional LES turbulence modeling. This model is known as *Implicit Large Eddy Simulation* (ILES).

It is now possible to understand the choice to use ILES as reference: there is no turbulence models, nor empirical equations which damage the solution, so we obtain reliable results without the inaccessible times of DNS.

2.3.4 Discretization

In order to get numerical results, it is necessary to the Navier-Stokes equations in both space and time domain, by approximating partial derivatives with finite differences. In particular, temporal derivatives become differences of successive instants of time, while spatial derivatives become differences of values of the adjacent grid nodes.

2.3.4.1 Spatial discretization

The convective terms in the Navier–Stokes equations are discretized using a hybrid energy-preserving/shock-capturing scheme in locally conservative form [6]. The one-dimensional convective flux (e.g. along x) f_x may be written as:

$$f_x = \rho u \varphi \tag{2.42}$$

where ρ is the density, u is the velocity and φ is the transported quantity. The numerical discretization of the streamwise flux derivative at the i-th node is expressed as:

$$\left.\frac{\partial f_x}{\partial x}\right|_i = \frac{1}{\Delta x}\left(\hat{f}_{x,i+1/2} - \hat{f}_{x,i-1/2}\right) \tag{2.43}$$

where Δx is the spacing of the mesh (grid-step), while $\hat{f}_{x,i+1/2}$ is the numerical flux defined at the intermediate nodes (Fig. 2.2).
The numerical flux may be written as

$$\hat{f}_{x,i+1/2} = 2\sum_{l=1}^{L} a_l \sum_{m=0}^{l-1} \left(\widetilde{\rho, u, \varphi}\right)_{i-m,l} \tag{2.44}$$

which is the conservative formulation. The a_l coefficients are the standard coefficients for central finite-difference approximations of the first derivative, while $2L$ is the order of accuracy. $\left(\widetilde{\rho, u, \varphi}\right)_{i-m,l}$, instead, is the two-point, three-variable discrete averaging operator, defined as:

$$\left(\widetilde{\rho, u, \varphi}\right)_{i,l} = \frac{1}{8}(\rho_i + \rho_{i+l})(u_i + u_{i+l})(\varphi_i + \varphi_{i+l}) \tag{2.45}$$

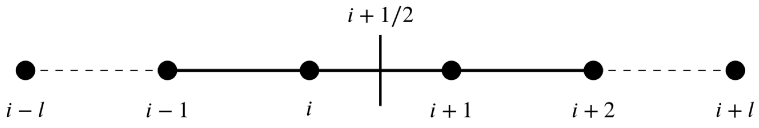

Figure 2.2: Scheme of the computational stencil in one space direction [6].

Central schemes are more efficient than schemes upwind and downwind (and even the most accurate), but they cannot describe shockwaves and may only be used in the smooth regions of the flow. When STREAmS detects a shock, it switches to generalized off-centered schemes in order to capture it. The locally conservative formulation allows direct hybridization of the

central flux with classical shock-capturing reconstructions, based on Lax–Friedrichs flux splitting[3][11]; the components of the positive and negative characteristic fluxes are reconstructed at the interfaces using a Weighted Essentially Non-Oscillatory (WENO) reconstruction. To judge on the local smoothness of the solution and switch between the two type of discretization, STREAmS relies on a modified version of the Ducros shock sensor[4] [6]:

$$\theta = \max\left(\frac{-\nabla\cdot u}{\sqrt{\nabla\cdot u^2 + \nabla\times u^2 + \frac{u_0^2}{L_0}}}, 0\right) \in (0,1) \tag{2.46}$$

where u_0 L_0 are the reference velocity and length. This sensor is designed to be $\theta \approx 0$ in smooth flow regions, and $\theta \approx 1$ in the presence of shockwaves. The viscous terms are expanded to Laplacian form and approximated with sixth order central schemes, to avoid odd–even decoupling phenomena. So, the numerical discretization of the spatial derivative in X-direction of the viscous fluxes at the i-th node is:

$$\left[\frac{\partial}{\partial x}\left(\mu\frac{\partial u}{\partial x}\bigg|_i\right)\right]_i = \frac{1}{\Delta x^2}\sum_{l=-L}^{L}\left(a_l^2\mu_{i+l}u_{i+l} + \mu_i b_l u_{i+l}\right) \tag{2.47}$$

where b_l coefficients are the finite-difference coefficients for the second derivative of order $2L$.

2.3.4.2 Time integration

From discretization of the spatial derivatives, we obtain a semi-discrete system of ordinary differential equations of the type [6]:

$$\frac{\delta \mathbf{w}}{\delta t} = \mathbf{R}(\mathbf{w}) \tag{2.48}$$

where $\mathbf{w} = [\rho, \rho u, \rho v, \rho w, \rho E]$ is the vector of the conservation variables and $\mathbf{R}$ is the vector of the residuals.
Time integration relies on a three stage, third order Runge-Kutta scheme, that is:

$$\mathbf{w}^{(l+1)} = \mathbf{w}^{(l)} + \alpha_l \Delta t \mathbf{R}^{(l-1)} + \beta_l \Delta t \mathbf{R}^{(l)} \quad , \quad l = 0,1,2 \tag{2.49}$$

where l is the sub-step, $\mathbf{w}^{(0)} = \mathbf{w}^n$ is the solution at n-th step, $\mathbf{w}^{(3)} = \mathbf{w}^{n+1}$ is the solution at (n+1)-th step and the integration coefficients are $\alpha_l = (0, 17/60, -5/12)$, $\beta_l = (8/15, 5/12, 3/4)$ [6].

[3]Lax-Friedrichs flux splitting consists of dividing flux into two components (up-wind propagation f^+ and down-wind propagation f^-) -so that $f(u) = f^+(u) + f^-(u)$- and then using the local maximum velocity of propagation as splitting elements. So, we can write this flux splitting method as: $f^{\pm}(u) = \frac{1}{2}\big(f(u) \pm \alpha u\big)$, with $\alpha = \max_u |f'(u)|$.

[4]See F. Ducros, V. Ferrand, F. Nicoud, C. Weber, D. Darracq, D. Gacherieu, T. Poinsot, "Large-Eddy Simulation of the Shock/Turbulence Interaction" J. Comput. Phys. 152 (2),1999, 517–549.

2.3.5 Immersed boundary method

The simulation used as reference consists of the solution of the flow around two bodies: capsule and parachute. Therefore, it is necessary to apply the boundary conditions (BCs) of *no-slip* and *no-penetration* on the surface of those bodies; we do it by applying the *Immersed Boundary Method*, also known simply as *IBM*.
The concept of IBM is that the solid surfaces of the immersed bodies do not coincide with the nodes of the computational grid, hence, instead of applying directly BCs (i.e. by setting $u = 0$), a fictitious force (f_{ibm}) is applied to the flow in the proximity of the interfaces, such that the flow is locally forced to move with the same local velocity of solid walls. If the relative velocity between the flow and the the body is zero, no-slip and no- penetration BCs are indirectly satisfied. The Navier-Stokes system is solved on a fixed grid -which does not conform to the immersed solid surfaces- to represent the dynamics of the flow:

$$\frac{\partial \rho}{\partial t} + \frac{\partial (\rho u_j)}{\partial x_j} = 0 \tag{2.50}$$

$$\frac{\partial (\rho u_i)}{\partial t} + \frac{\partial (\rho u_i u_j)}{\partial x_j} + \frac{\partial p}{\partial x_j} - \frac{\partial \sigma_{ij}}{\partial x_j} - \rho f_{ibm} = 0 \tag{2.51}$$

$$\frac{\partial (\rho e)}{\partial t} + \frac{\partial (\rho e u_j + p u_j)}{\partial x_j} + \frac{\partial q_j}{\partial x_j} - \frac{\partial (\sigma_{ij} u_i)}{\partial x_j} - \rho f_{ibm} u_i = 0 \tag{2.52}$$

In particular, $f_{ibm} = f_{ibm}(x_i, t)$.
IBM is divided into two main groups: *continuous forcing* method and *discrete forcing* method. The first one is represented in the 2.51 system and it is accurate and straight-forward to implement, but it works with Dirichlet BCs only. Therefore, since compressible Navier-Stokes equations require both Dirichlet and Neumann boundary conditions, it is necessary to use the discrete forcing method, which which is able to work with both BCs. This method may be *direct* or *indirect*: the second one exploits a force distribution function, which introduces a spreading effect on the interfaces (undesirable when great accuracy is needed). The direct boundary conditions imposing is applied through the Ghost Point Forcing Method (GPFM), allowing a sharp representation of the body surface [11].

2.3.5.1 Ghost Point Forcing Method

The method is more suitable for the applications where the natural boundary conditions are specified as a gradient of some fluid variables as in thermal and compressible flows problems. It needs to discern if a computational node is a fluid, a ghost, or a solid one and to pursue this target, some automatic solid-detection techniques must be employed (e.g. ray tracing algorithm). Thus, the boundary can not be represented by a collection of Lagrangian points, but the surface must be discretized by a mesh with elements like triangles in 3D cases.

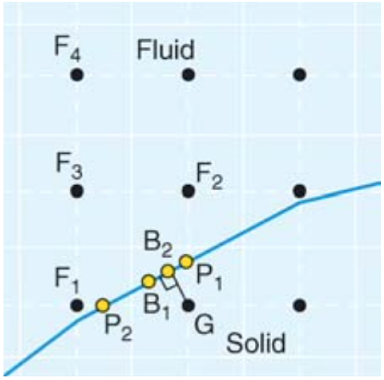

Figure 2.3: Representation of the points in the proximity of an immersed boundary (GPFM schematic representation). F_i are fluid points, G is the ghost point, and B_i and P_i are locations where the boundary condition can be enforced [18].

The imposition of boundary conditions on the surface is implemented through the use of *ghost cells* that are cells in the solid that have at least one neighbor in the fluid. Hence, a ghost region is created adjacent to the immersed boundary: ghost nodes within the ghost region must be as many as required by the accuracy order of finite-difference scheme utilized by the solver. Since in this work we employ sixth-order schemes, the number of ghost nodes is set to six.

2.4 Modal analysis for fluid flows

Modal decomposition is used to extract energetically (and dynamically) important features from data sets, such as fluid flows.. That spatial features are called *modes* and they are accompanied by characteristic values, representing either the energy content levels or growth rates and frequencies. These modes can be determined from the flow-field data or from the governing equations [26].
Modal analysis methods for fluid flows extract the important oscillatory modes of the flow and, as shown in figure 2.4, two of these most dominant modes and the mean represent (reconstruct) the flow-field very effectively. Others additional modes may be added to reconstruct the original flow more accurately, but their contributions are much smaller than the two unsteady modes shown in this example.
There are a lot of modal analysis methods which are growing and developing -e.g. Singular Value Decomposition (SVD), Eigenvalue Decomposition, Proper Orthogonal Decomposition (POD), Dynamic Mode Decomposition (DMD), balanced POD, Eigensystem Realization Algorithm (ERA) and others [23]-, but in this work, we have focused on POD method. Before explaining the used method, we take a look to the Eigenvalue Decomposition and the SVD, then the POD.

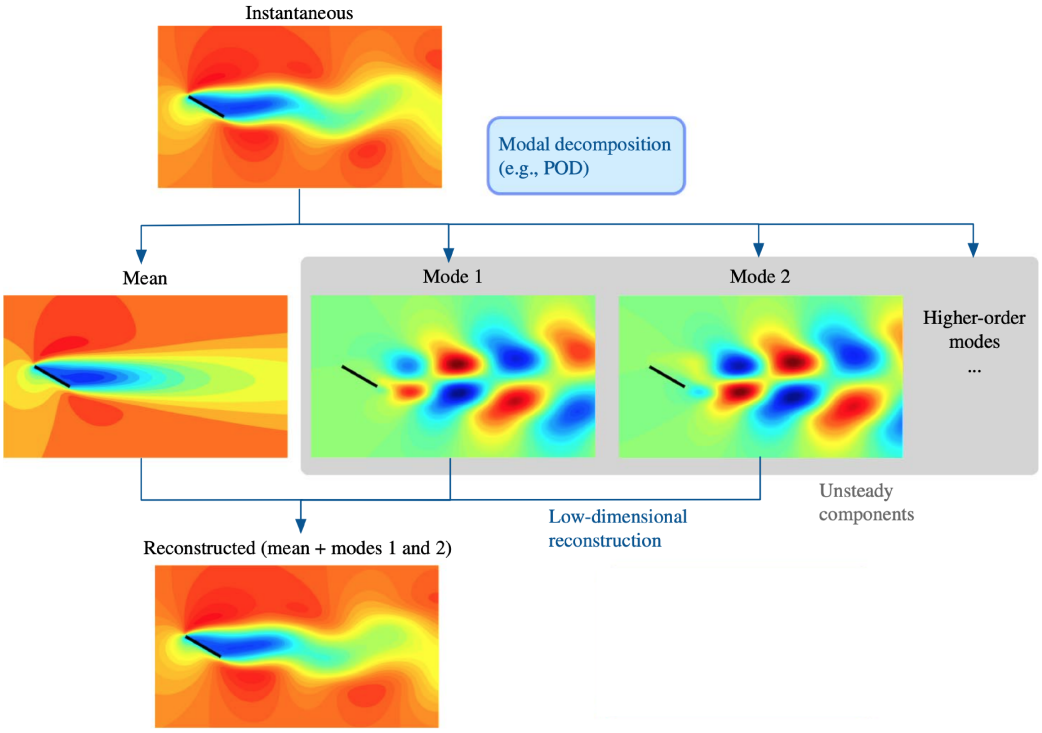

Figure 2.4: Example of a POD reconstruction of a two-dimensional incompressible flow over a flat-plate wing [26]. This example is only meant to show how a complex non-linear separated flow is well represented by only two POD modes.

2.4.1 Eigenvalue decomposition

Eigenvalue decomposition is performed on square matrices and it is usually employed when the range and domain of the matrix are the same.
The classical eigenvalue expressions [26] [29] is:

$$\mathbf{A}\mathbf{v} = \lambda\mathbf{v} \tag{2.53}$$

where:

- $\mathbf{A} \in \mathbb{C}^{n\times n}$ is a matrix;
- $\mathbf{v} \in \mathbb{C}^n$ is the *eigenvector*;[5]
- $\lambda \in \mathbb{C}$ is the *eigenvalue*[6] and it is scalar.

If $\mathbf{A}$ has n linearly independent eigenvectors $\mathbf{v}_j$ (so, there will be λ_j eigenvalues, with $j = 1, \ldots, n$), we can modify equation 2.53 into:

$$\mathbf{A}\mathbf{V} = \mathbf{V}\Lambda \tag{2.54}$$

[5] If $\mathbf{v}$ is an eigenvector, also $\alpha\mathbf{v}$ is an eigenvector, with $\alpha \in \mathbb{C}$.
[6] The set of all eigenvalues of $\mathbf{A}$ is called *spectrum* of $\mathbf{A}$.

where $\mathbf{V} = [\mathbf{v}_1, \ldots, \mathbf{v}_n] \in \mathbb{C}^{n\times n}$ and $\Lambda = diag(\lambda_1, \ldots, \lambda_n) \in \mathbb{C}^{n\times n}$.
Hence, we obtain the *eigenvalue decomposition* simply post-multiplying $\mathbf{V}^{-1}$ to the 2.54 equation:

$$\mathbf{AV} = \mathbf{V}\Lambda\mathbf{V}^{-1} \tag{2.55}$$

It is important that $\mathbf{A}$ is composed of a full set of n linearly independent eigenvectors, in order that eigenvalue decomposition is applicable.
Now, assuming that the quantities of interest (e.g. velocity) at a particular time have been discretized and assembled into a vector $x(t)$; this vector is called the *state vector*. For linear dynamical systems $x(t) \in \mathbb{C}^n$ is described by the following equation:

$$\dot{\mathbf{x}}(t) = \mathbf{A}\mathbf{x}(t) \quad \longrightarrow \quad \mathbf{x}(t) = \exp(\mathbf{A}t)\mathbf{x}(0) = \mathbf{V}\exp(\Lambda t)\mathbf{V}^{-1}\mathbf{x}(0) \tag{2.56}$$

where $\mathbf{x}(0)$ is the initial condition.
The eigenvalues λ_j are composed by the real part, which represents the growth (or decay) rate and the imaginary part, that is the frequency at which $\mathbf{x}(t)$ evolves in the direction of the eigenvector. These two parts denote the dynamic behavior of the system, which might be:

- unstable $\longrightarrow$ if $Re(\lambda_j) > 0$
- metastable $\longrightarrow$ if $Re(\lambda_j) = 0$
- stable $\longrightarrow$ if $Re(\lambda_j) < 0$

So, for a linear system to be stable, i.e. each mode tends to dampen, it is necessary that $Re(\lambda_j) < 0$ for each j (figure 2.5).

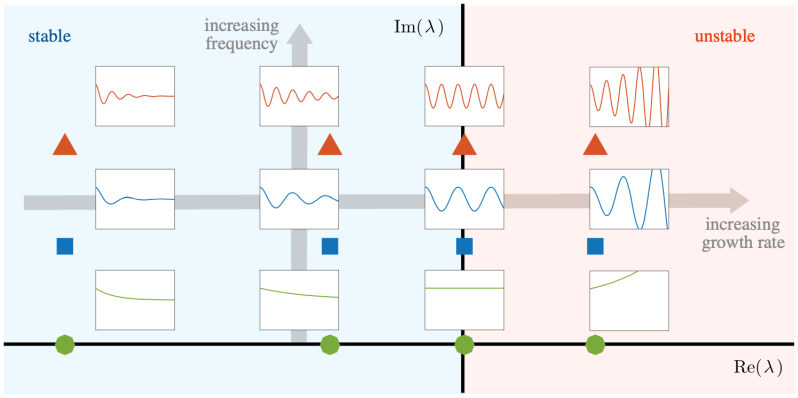

Figure 2.5: Schematic of the dynamic stability of a system, characterized by the eigenvalues. Representation over the imaginary plane [26].

2.4.2 Singular Value Decomposition

Singular value decomposition (SVD) can be applied on rectangular matrices; furthermore SVD shows how a rectangular matrix stretches and rotates a vector -thus domain and range

spaces are not necessarily the same.
Let's consider the complex rectangular matrix $A \in \mathbb{C}^{m\times n}$, the unit vectors $\mathbf{v}_j \in \mathbb{C}^n$ and $\mathbf{u}_j \in \mathbb{C}^m$ and the magnitudes σ_j. Between them we can write the following relation

$$\mathbf{A}\mathbf{v}_j = \sigma_j \mathbf{u}_j \tag{2.57}$$

which may be re-write in matrix form as:

$$\mathbf{AV} = \mathbf{U\Sigma} \tag{2.58}$$

where $\mathbf{V} = [\mathbf{v}_1, \ldots, \mathbf{v}_n] \in \mathbb{C}^{n\times n}$ and $\mathbf{U} = [\mathbf{u}_1, \ldots, \mathbf{u}_n] \in \mathbb{C}^{m\times m}$ are *unitary matrices*[7], while $\mathbf{\Sigma} \in \mathbb{R}^{m\times n}$ is a diagonal matrix with $\sigma_1 \geq \cdots \geq \sigma_p \geq 0$ along its diagonal, with subscript $p = \min(m, n)$. Now we can multiply equation 2.58 for $\mathbf{V}^*$ and obtain the singular value decomposition, defined as:

$$\mathbf{A} = \mathbf{U\Sigma V}^* \tag{2.59}$$

The column vectors $\mathbf{u}_j$ and $\mathbf{v}_j$ are called respectively *left singular vectors* and *right singular vectors*; both of them can be determine up to a complex scalar of magnitude one. An example of SVD may be represented by the following figure 2.6, which shows how this decomposition can stretch and rotates a vector:

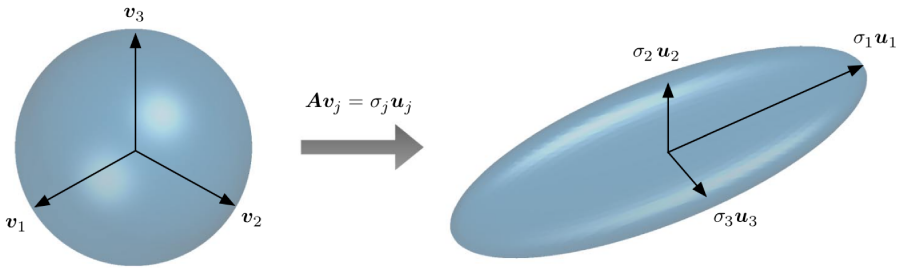

Figure 2.6: Representation of the stretching of a sphere via singular value decomposition. Example with $\mathbf{A} \in \mathbb{R}^{3\times 3}$ [26].

So, we can imagine SVD as a tool that represents the effect of matrix operation through the multiplication by scalars (which are the singular values), given the appropriate directions. Because SVD is applied to a rectangular matrix, we need two sets of basis vectors to span the domain and range of the matrix. Thus, the left singular vectors $\mathbf{U}$ span the range of $\mathbf{A}$ (which may be interpret as way to assign the grid-point in the discrete fluid-flow domain), while the right singular vectors $\mathbf{V}$ span the domain of $\mathbf{A}$ (that can be interpret as way to assign the temporal coefficient in the discrete fluid-flow domain). This is the bigger difference between SVD and eigenvalue decomposition because in the second one, domain and range are generally the same.

[7]Unitary matrix means that a general matrix satisfies $X^* = X^{-1}$, where "$*$" indicates the conjugate transpose.

2.4.3 Proper Orthogonal Decomposition

The proper orthogonal decomposition (POD) determines the optimal set of modes to represent data, based on L_2 norm, that is the energy. The goal of POD is to decompose a set of data into a minimal number of basis functions or modes to capture as much energy as possible; so we call the modes of this modal decomposition technique as *energy modes*.
Assume that the unsteady component of the vector field may be decomposed as the difference between a vector field $\mathbf{q}(\xi, t)$ (e.g. velocity) and its temporal average $\bar{\mathbf{q}}(\xi)$, so that:

$$\mathbf{q}(\xi, t) - \bar{\mathbf{q}}(\xi) = \sum_j a_j \phi_j(\xi, t) \tag{2.60}$$

$\phi_j(\xi, t)$ are the modes, a_j are the expansion coefficients, ξ is the spatial vector and t is the time. Equation 2.60 represents the flow-field in terms of generalized Fourier series for some set of basis function, as $\phi_j(\xi, t)$ are, and we clearly searching for the optimal set of basis functions for the given stream data. This approach led to modes which are functions of space and time (or even frequency). As for the aeroelasticity methods [29], we can decompose the right hand side of the previous equation 2.60 in order that the expansion coefficients a_j will be time-dependent, while the modes will be only space-dependent (so they will be spatial modes). Re-writing the equation we obtain:

$$\mathbf{q}(\xi, t) - \bar{\mathbf{q}}(\xi) = \sum_j a_j(t) \phi_j(\xi) \tag{2.61}$$

It is noticeable that the fluctuations in the original field are re-defined as a linear combination of the modes and their corresponding temporal coefficients. The inputs are *snapshots* of scalar (e.g. pressure) or vector (e.g. velocity) field $\mathbf{q}(\xi, t)$, over up to three-dimensional discrete spatial points ξ at discrete times t_i. Instead, the outputs are a set of orthogonal modes $\phi_j(\xi)$ with their corresponding temporal coefficients $a_j(t)$ and the energy levels λ_j (which are arranged in the order of their relative amount of energy). We mean there are three outputs: the matrix of modes, the matrix of temporal coefficients and the matrix of the energy.
There are two main approaches to fulfill the POD of the fluid-flow data:

- spatial POD method;
- snapshot POD method;

2.4.3.1 Spatial pod method

This approach is also called *classical* POD method and it starts from the preparation of the flow-field snapshots (where the flow-field is $\mathbf{q}(\xi, t)$), in order to obtain a collection of column vectors $\mathbf{x}$(t). These vectors are the fluctuations of the fluid-flow and we can express them -considering a collection of finite dimensional data vectors- as:

$$\mathbf{x}(t) = \mathbf{q}(\xi, t) - \bar{\mathbf{q}}(\xi) \in \mathbb{R}^n \quad , \quad t = t_1, \ldots, t_m \tag{2.62}$$

In order to find the optimal basis vectors that can best represent the given data, we are searching for $\phi_j(\xi)$ such that $\mathbf{q}(\xi)$ is represented in an optimal way and with the least number of modes. So, we need modes with the maximum energy content so that we can use minimum number of them. It is possible to do it by calculating the eigenvalues λ_j and the eigenvectors ϕ_j:

$$R\phi_j = \lambda_j \phi_j \quad , \quad \phi_{\mathbf{j}} \in \mathbb{R}^n \ , \ \lambda_1 \geq \cdots \geq \lambda_n \geq 0 \tag{2.63}$$

In this case, eigenvalues are in descending order: since each eigenvalue represents the growth (or decrease) rate along one direction, the bigger the mode, the more important it is from an energy point of view.
R is defined as the covariance matrix[8] of vector $\mathbf{x}$(t):

$$R = \sum_{i=1}^{m} \mathbf{x}(t_i)\mathbf{x}^T(t_i) = XX^T \in \mathbb{R}^{n\times n} \tag{2.64}$$

where X is the matrix which represents the m snapshot data that are stacked into a matrix form:

$$X = [\mathbf{x}(t_1)\ \mathbf{x}(t_2)\ \ldots\ \mathbf{x}(t_m)] \in \mathbb{R}^{n\times m} \tag{2.65}$$

X is essentially a matrix made by stacking all the points of the domain in columns and flanking them with the different snapshots/time-steps m. The size of the covariance matrix depends by the spatial degrees of freedom of the data: in fluid-flow application, that data-size n is generally equal to the number of grid points, multiplied by the number of variables to be considered in the data.
The eigenvectors $\phi_{\mathbf{j}}$ are called *POD modes* and they are orthonormal; so it means that scalar product between the modes satisfies the following condition:

$$\langle \phi_{\mathbf{j}}, \phi_{\mathbf{k}} \rangle \equiv \int_V \phi_{\mathbf{j}} \cdot \phi_{\mathbf{k}}\, dV = \delta_{jk} \quad , \quad j,k = 1,\ldots,n \tag{2.66}$$

where $\delta_{jk} = 0$ if $j \neq k$. It notice that we consider that the flow-field data are placed on a uniform grid, such that scaling due to the size of the cell volume, does not need to be taken into account[9] [26]. So, the eigenvalues λ_k indicate how much each eigenvector ϕ_k captures the original data in the L_2 norm sense,[10] scaled by m. If velocity vector is associated to $\mathbf{x}$(t), the calculated eigenvalues coincide to the kinetic energy captured by the POD modes. Thanks to this correspondence, we may use the eigenvalues to determine the optimal modes number (r), necessary to represent the fluctuations in the fluid-flow data. In order to satisfy

[8] Covariance matrix is defined as $R = XX^T/m$: just not to burden the writing, we lump the factor $1/m$ in the eigenvalues.

[9] If we consider the size of the cell volume, the covariance matrix should be written as $R = XX^TW$, where W contains the spatial weights. The same approach is used for the 2.4.3.2 paragraph where, in the equation 2.70, matrix X^TX should be X^TWX.

[10] We remember that L_2 norm is defined as $\|f\| = \sqrt{\sum_i f_i^2}$

this requirement, we have to obtain

$$\frac{\sum_{j=1}^{r} \lambda_j}{\sum_{j=1}^{n} \lambda_j} \approx 1 \tag{2.67}$$

which means that the partial/total energy ratio must be similar to one.
So, it is possible to re-define the fluctuations of the fluid-flow in terms of the truncated (and so finite) series as:

$$\mathbf{q}(\xi, t) - \bar{\mathbf{q}}(\xi) \approx \sum_{j=1}^{r} a_j(t)\phi_j(\xi) \tag{2.68}$$

It is clear the power of this result: we reduce the high-dimensional (n) flow-field into only r modes, which represent it.
The temporal coefficients $a_j(t)$ may be calculated by:

$$a_j(t) = \langle \mathbf{x}(t)\,,\, \phi_j(\xi) \rangle \quad , \quad \mathbf{x}(t) = \mathbf{q}(\xi, t) - \bar{\mathbf{q}}(\xi) \tag{2.69}$$

2.4.3.2 Snapshot POD method

The snapshot POD method is used when the spatial size of the data (n) is very broad. Because of the covariance matrix $R = XX^T$ is an $n \times n$ matrix, evaluating the eigenfunctions using the spatial POD method is unrealizable. This method takes a collection of snapshots $\mathbf{x}(t_i)$ at discrete time levels t_i, ($i = 1, \ldots, m$, with $m \ll n$) and it solves an eigenvalue case of a narrower size ($m \times m$) to find the POD modes. The number of snapshots (m) must be defined such that principal fluctuations of the flow-field are well resolved in time. In order to be more formal, we can write:

$$X^T X \psi_j = \lambda_j \psi_j \quad , \quad \psi_j \in \mathbb{R}^m \quad , \quad m \ll n \tag{2.70}$$

where $X^T X$ is an $m \times m$ matrix (instead of $n \times n$) and ψ_j are the eigenvectors of the "reduced" eigenvalues. From these eigenvectors, POD modes may be recovered by

$$\phi_j = X\psi_j \frac{1}{\sqrt{\lambda_j}} \in \mathbb{R}^n \quad , \quad j = 1, \ldots, m \tag{2.71}$$

and it may be written in the matrix form as:

$$\mathbf{\Phi} = \mathbf{X}\mathbf{\Psi}\mathbf{\Lambda}^{-1/2} \tag{2.72}$$

where:

- $\mathbf{\Phi} = [\phi_1\, \phi_2\, \ldots\, \phi_m] \in \mathbb{R}^{n \times m}$
- $\mathbf{\Lambda} = [\lambda_1\, \lambda_2\, \ldots\, \lambda_m] \in \mathbb{R}^{m \times m}$

This method is widely used for the fluid-mechanics problems because, since those problems are high-dimensional data, it allows to get a big reduction in the required computation and

memory resources, which means a huge decrease of calculation time.

2.5 Simulation setup

The reference Large-Eddy simulation was computed using the in-house compressible flow solver STREAmS developed by Bernardini et al.[6], 2021 at "La Sapienza", University of Rome. STREAmS (Supersonic TuRbulEnt Accelerated navier-stokes Solver) implements advanced numerical methods based on finite difference energy preserving schemes with integrated WENO algorithms.
Inside the domain of the simulation there are two bodies, which are the capsule and the trailing parachute; the simulation specifications are based on the ESA's ExoMars 2022 mission. The two bodies are constrained to their domain position; the parachute structure is rigid (Figure 2.7). The reference system of coordinates is located on the leading edge of the capsule (i.e. it is situated on the capsule nose), with the x-axis on the system symmetry axis. In this work, suspension lines are not considered because their effect on the flow field (if considering their diameter) may be considered negligible [10] [30]. The dimensions of the capsule and the parachute are shown in the following figure 2.8.

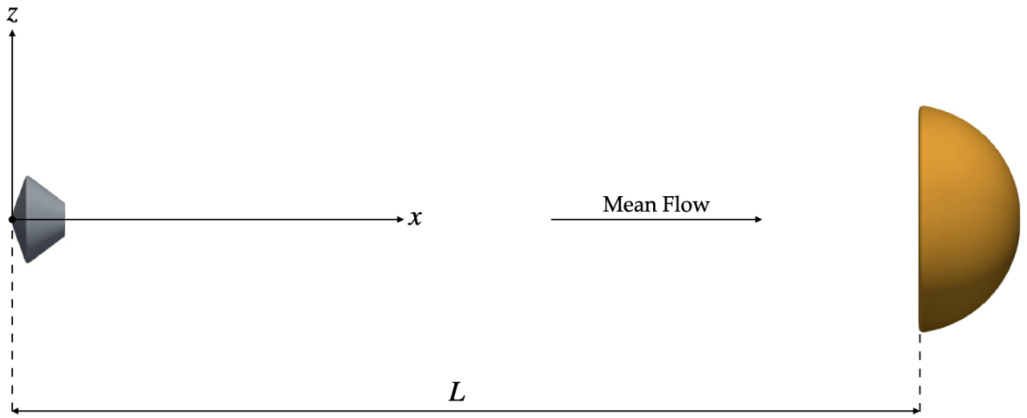

Figure 2.7: Capsule-parachute system, two-dimensional view on (x, z) plane.

The capsule is a scaled version of ExoMars 2022 descent module, with a maximum diameter $D = 3.8\,m$, a height $h = 0.61D = 2.32\,m$ and an aeroshell half-angle equal to 70°. The distance from the capsule tip to the parachute leading edge is called *trailing distance* and it is $L = 10D$. ExoMars trailing distance is $L_e = 1.5L$: we choose a lower value in order to emphasize the capsule-parachute interaction [25].
The parachute is inspired by the *Disk Gap Band* (or simply *DGB*) configuration, but without the band; moreover, the hole on in its apex is known as *vent*. This choice is owed to the fact that we want to emphasize the effects of the breathing cycle, which are reduced by the presence of the band of the DGB.

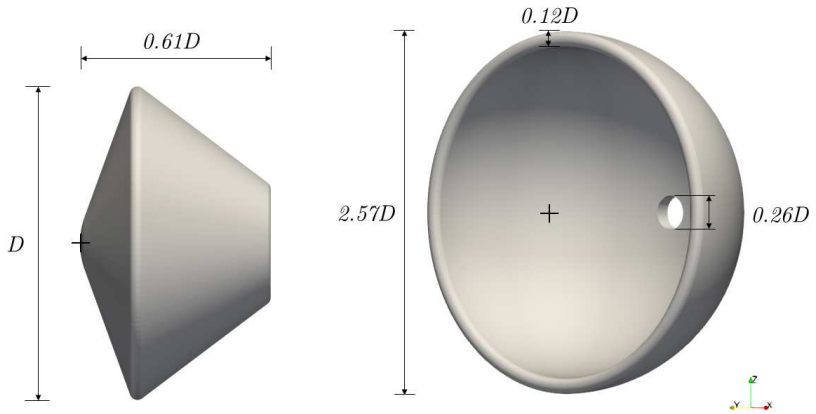

Figure 2.8: Dimensions of capsule and parachute, not to scale.

The typical *inflation ratio* of a DGB parachute is $D_e/D_0 = 0.65$, where D_e is the the projected diameter of the inflated parachute and $D_0 = 15\,m$ (nominal diameter) is a fictitious diameter obtained by assuming that the nominal area of the canopy is a circle [7] [9]; thus, the diameter of the inflated parachute results $D_e = 9.75\,m$. Normalizing D_e by D (maximum capsule diameter), we obtain that the maximum dimensionless diameter of the inflated canopy is $D_p = 2.57$. In order to get results for the parachute, it was designed with an increased thickness of 0.12 (in non-dimensional term) and with a rounded leading edge.[11]
In the same way of D_p, we normalized the diameter of the vent D_v, so that $D_v = 0.26$.

2.5.1 Computational LES domain

The non-dimensional dimensions -and their respective coordinates- of the LES domain are:

- $L_x = 20D \quad \longrightarrow \quad$ [-1;19]
- $L_y = 10D \quad \longrightarrow \quad$ [-5;5]
- $L_z = 10D \quad \longrightarrow \quad$ [-5;5]

In the following figure 2.9 it is shown the domain; as already said, the origin of the coordinates system is centered on the capsule tip:

[11] During the simulation, if an object is smaller than the ghost region, it cannot be simulated, as in the case of cables; this is why we have increased the parachute thickness.

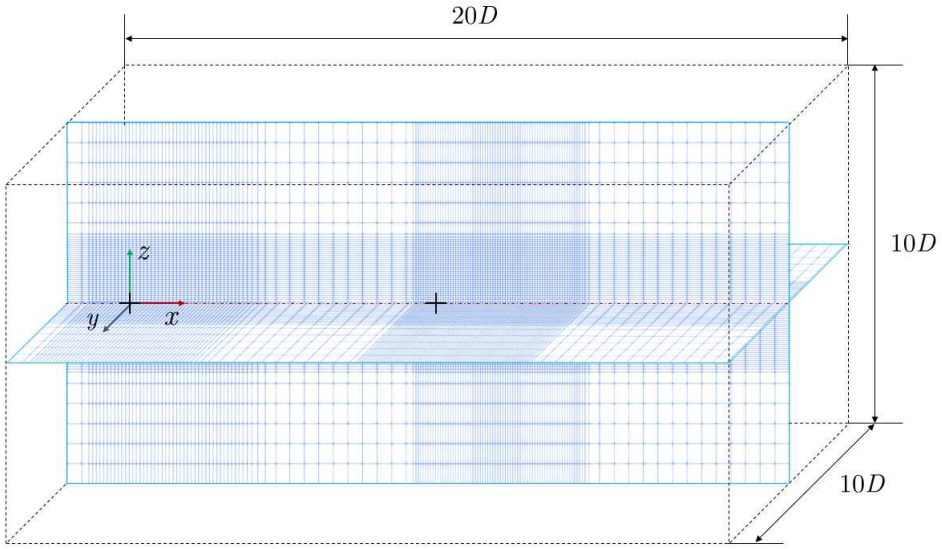

Figure 2.9: Representation of the 3D domain of the LES simulation.

The number of the grid nodes is set as: $N_x = 2560$, $N_y = 840$, $N_z = 840$, where N_x, N_y and N_z are respectively the number of points on the x, y and z direction. This grid is a rectangular elements structured grid, increases its density toward the center of the domain, in order to satisfy the local requirement. For example, flow regions near the solid bodies are provided with the finest resolution to better describe the fluid-solid interaction, while the frontier zone is less dense. Considering the x direction, capsule and parachute regions have a *contraction factor* equal to 0.2: this means that the grid-step is $0.2\Delta_0$, where $\Delta_0 = L_x/N_x$ is the reference value of the grid-step. Grid-step varies from Δ_0 to $0.2\Delta_0$ sharply in front of the bodies, while smoothly behind the bodies. In fact, bow shocks are in proximity to the bodies, while the turbulent wake (that requires a fine resolution) extends over a long distance behind the bodies. The refinement along y and z directions ensures that the region around the symmetry axis has the best resolution: along both y and z axis, contraction factor is 0.3 and symmetrical with respect to x axis.
Simulations are performed on CINECA's *Marconi100* cluster, using the parallelization of the domain on 64 GPUs.

2.6 Grid uniformity

Every discrete analysis requires a grid on which to unfold the calculations. The domain taken for the POD reconstruction is smaller than the entire LES domain because, in this work, we are analyzing the parachute behavior only; hence, we cut the domain in order to reduce the calculation time and to focus on the canopy. In particular, we change the dimensions of the grid as it shown in the following table 2.1; note that there is no Y/D dimension for POD analysis because we calculated the reconstruction on a 2D domain.

Dimension	LES		POD
X/D	20	$\rightarrow$	12
Y/D	10	$\rightarrow$	-
Z/D	10	$\rightarrow$	4.5

Table 2.1: Non-dimensional LES and POD grid size

Consider now the 2D grid for both LES and POD. The grid of the LES is quite uniform because it is divided in 9 zones:

- Five uniform zones where grid elements are constant;
- Four zones where grid elements are gradually changing their size.

These 4 regions are small and hypothetically negligible, in fact their sum covers about 3% of the entire domain, in particular, these four regions are allocated at these positions:

- before the capsule, at $X/D = -0.5$;
- behind the capsule, at $X/D = 4.5$;
- in front of the parachute, at $X/D = 8.5$;
- after the parachute, at $X/D = 13.5$.

Nevertheless, in order to obtain more valid results we calculated the area of each grid element and we evaluate the variation of it. These areas were calculated by creating a second fictitious grid, where X and Z dimensions correspond to the distance between two adjacent nodes; this distribution of values associated to each node can be considered as a scalar field which represent the rate of change in the dimensions of the grid cells. An important detail is in the correspondence of borders of the domain: on these positions, with this method, we do not consider the last grid cell; however, this does not represent a relevant issue given the position of the parachute, which is located in the middle of the control area.
To obtain a meaningful value, these areas were normalized by the average value of the area of the all grid cells, in order to assess the change of every cell, compared to a reference value. In particular, what was important to assess was not the absolute rate of change, but the non-dimensional area variation between two adjacent cells.

3 | Results

In the following chapter we present the results obtained from the modal reconstruction of the POD technique, applied to the baseline Large-Eddy Simulation introduced in the previous pages.
First, we analyze the energy modes and their fluctuations; the reconstructed flow field are then compared with the original LES data, both using one-dimensional profiles and via root-mean-square evaluation of the averaged fluctuations. The effect of grid uniformity is briefly considered at the end in order to assess its influence on the accuracy of final results.
LES domain is three-dimensional, while POD domain is defined in the two-dimensional XZ section, extracted from the whole computational space. In the following figures 3.1 and 3.2 there are a representation of the all capsule-parachute domain (two-dimensional y=0 section obtained from the LES three-dimensional field); in particular, we represent the instantaneous and mean density field and the instantaneous and mean non-dimensional X-momentum field:

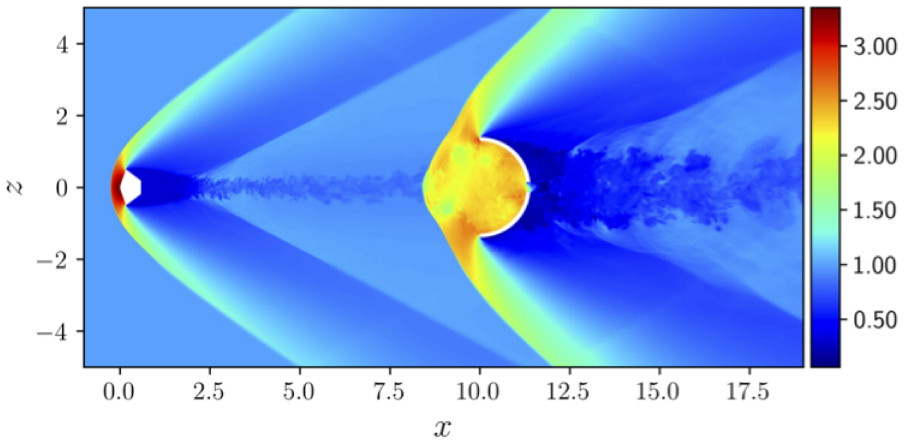

(a) Instantaneous 2D density

Figure 3.1: Capsule-Parachute 2D domain: instantaneous and mean density.

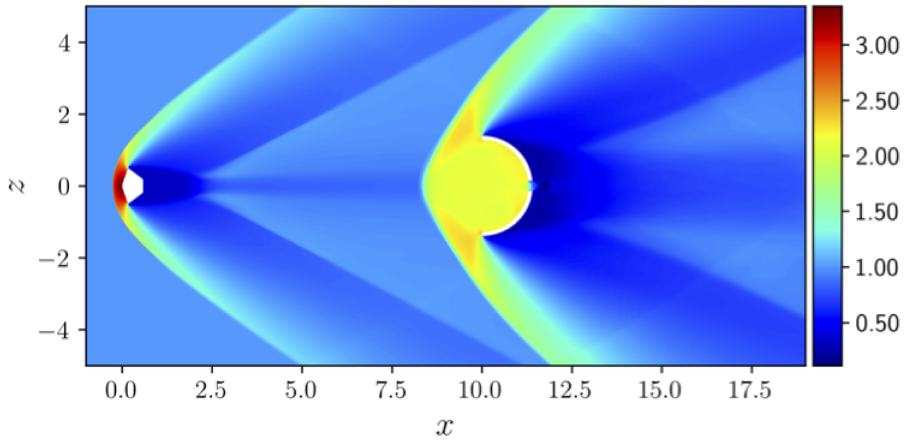

(b) Mean 2D density

Figure 3.1: Capsule-Parachute 2D domain: instantaneous and mean density.

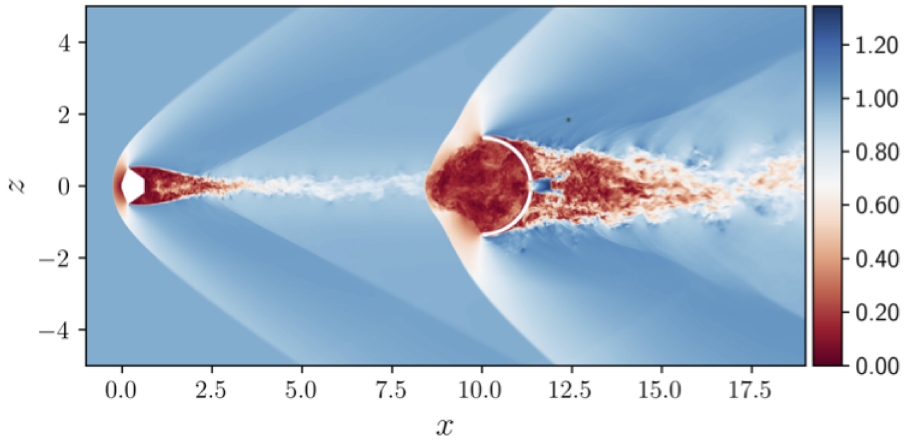

(a) Instantaneous 2D X-momentum

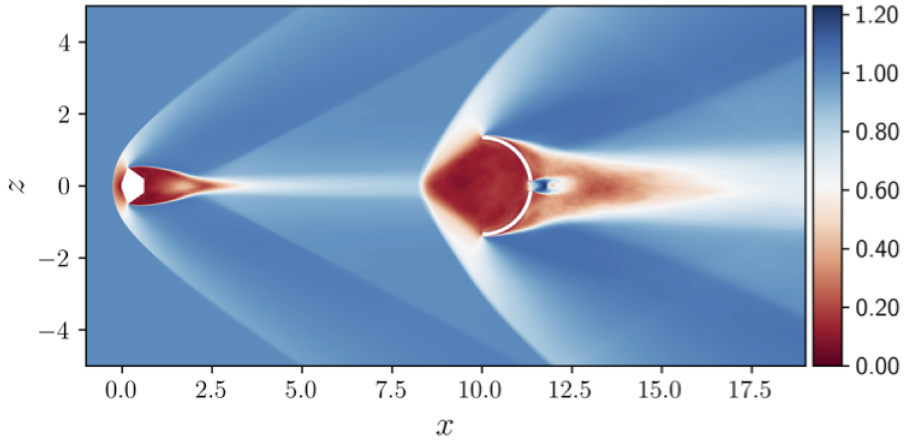

(b) Mean 2D X-momentum

Figure 3.2: Capsule-Parachute 2D domain: instantaneous and mean dimensionless X-momentum.

3.1 Energy modes field

In order to obtained a reasonable amount of energy in the reconstruction, we combinated a total of ten POD modes, as described previously at 2.4.3 paragraph. In this way, we obtain more than 74% of the total energy, with 150 snapshots taken, in an observation window that ranges from $t/t_0 = 52$ to 56. From this condition, we start to validate the obtained results by POD reconstruction.

It is important to highlight that each mode of POD reconstruction does not contain only one frequency, but it stores different frequencies which the same energy content. The energy fluctuations contained in these different modes are related to the turbulence kinetic energy of the real flow; in particular with this reconstruction we find the average patterns of oscillations and show them through different energy modes.

In the following figure 3.3 are shown the 10 energy modes calculated by our reconstruction. In each representation we can distinctly observe the shape of the front shock wave: this is due to the strong fluctuation that moves the discontinuity and cause the ”breathing” phenomenon. This results would not be visibile if there were no capsule wake, since the shock motion is intrinsically connected to the turbulence ingestion that is produced from the descent module positioned in the front. This motion of instability is the *breathing cycle instability.*

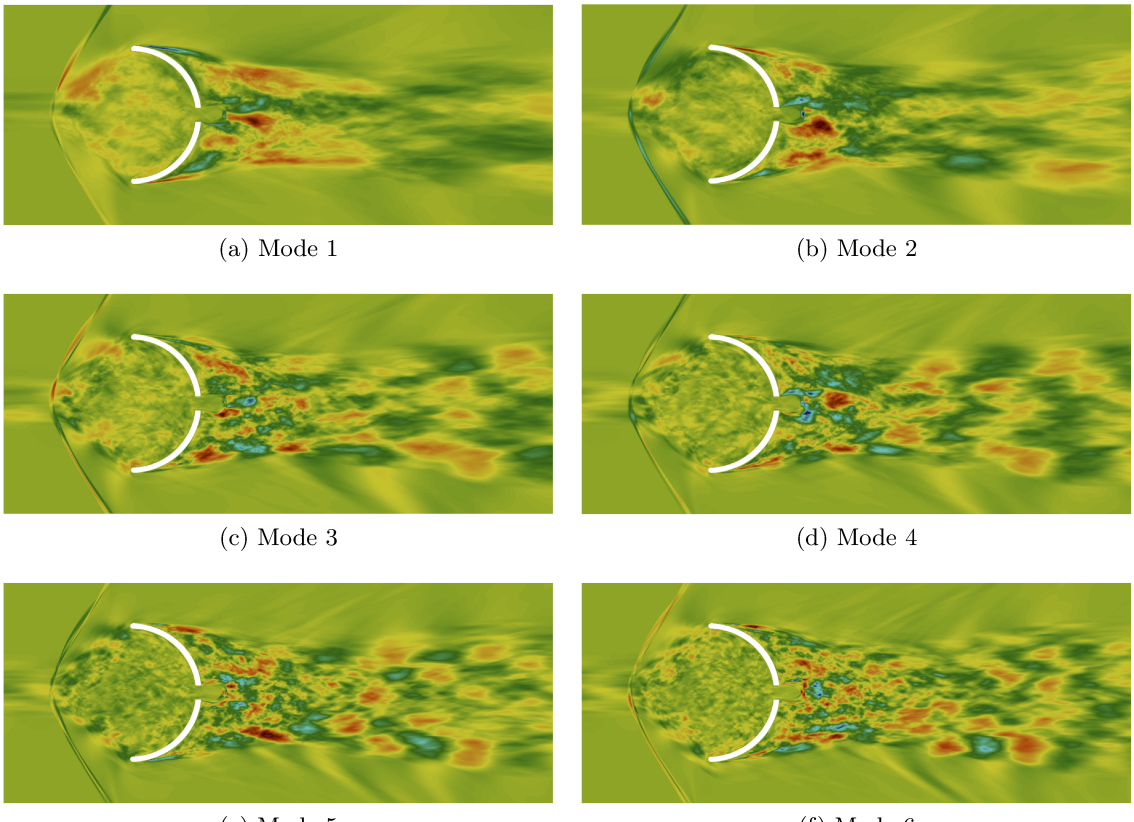

(a) Mode 1 (b) Mode 2

(c) Mode 3 (d) Mode 4

(e) Mode 5 (f) Mode 6

Figure 3.3: First 10 energy modes.

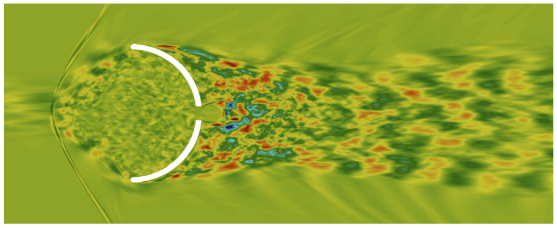

(g) Mode 7

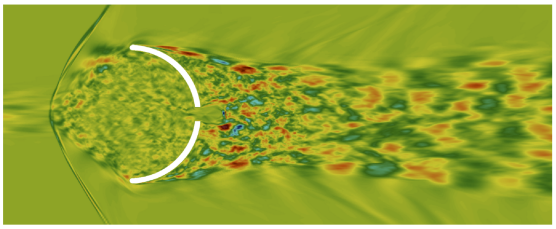

(h) Mode 8

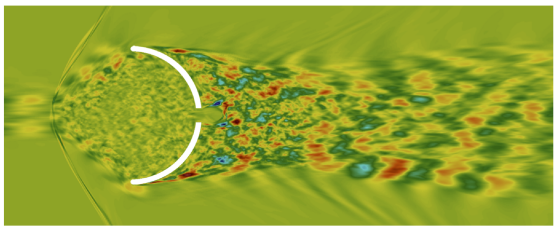

(i) Mode 9

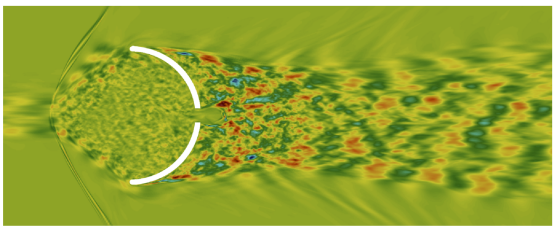

(j) Mode 10

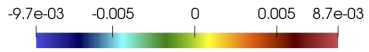

(k) Legend

Figure 3.3: First 10 energy modes.

As we explain in 2.4.3.1 section, the first mode is the one with the higher energy content; a common feature of each mode is the large energy variation behind the parachute, where the wake develops; this is due to the separation of boundary layer, which generates vortex structures. We can also see that there is a slight sort of symmetry in the wake; this symmetry is lost as we move toward the inlet of the canopy, after the shock wave.
In order to better evaluate the differences connected to the energy modes, one-dimensional profiles along the axial direction are proposed in the following section.

3.1.1 Energy fluctuation

In the following pictures, we present one-dimensional profiles along the axial direction of the energy connected of each selected POD mode.

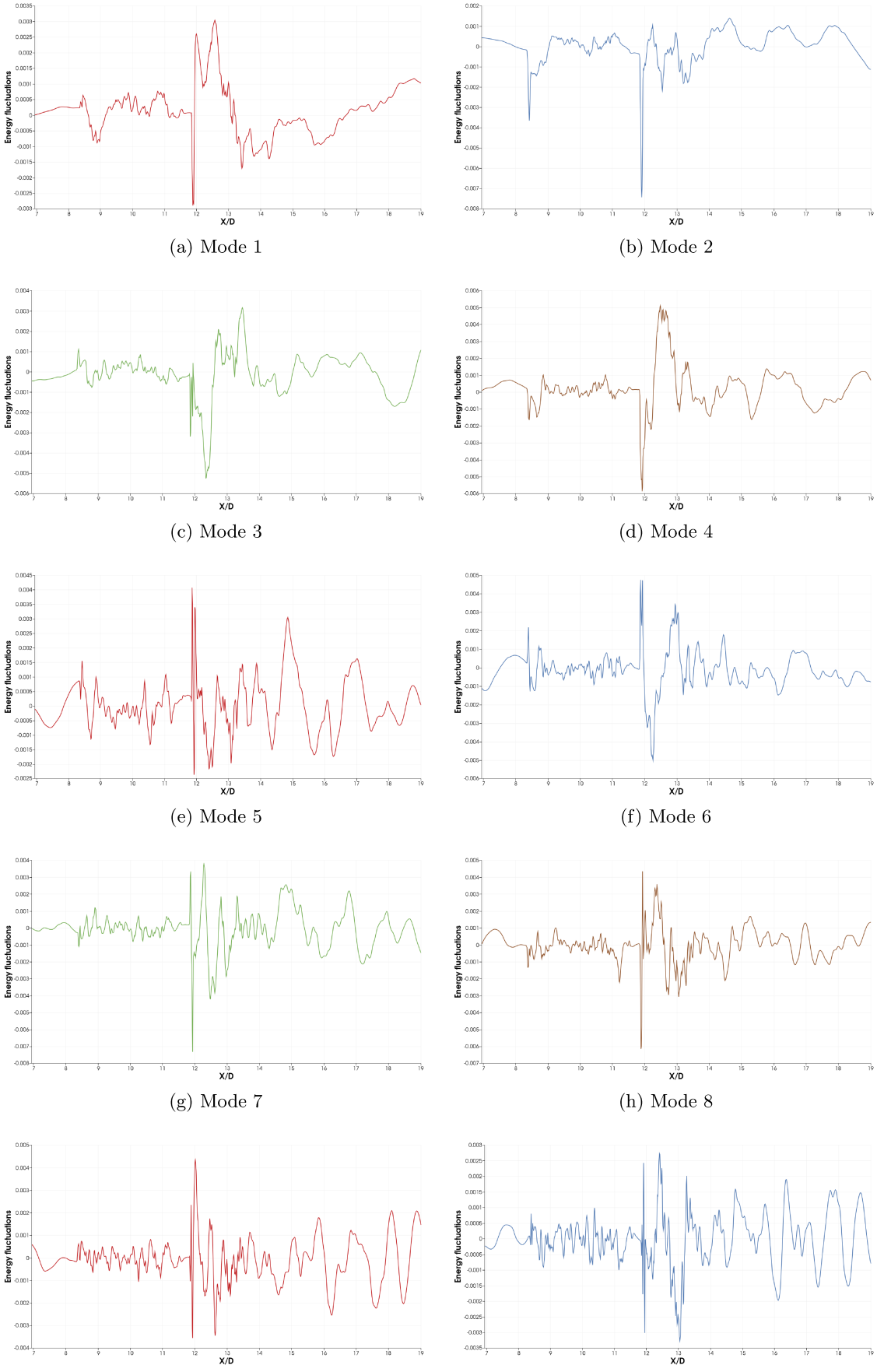

(a) Mode 1

(b) Mode 2

(c) Mode 3

(d) Mode 4

(e) Mode 5

(f) Mode 6

(g) Mode 7

(h) Mode 8

(i) Mode 9

(j) Mode 10

Figure 3.4: Energy fluctuation of the energetic modes.

These plots of figure 3.4 show the fluctuations of energy modes around the parachute. In this way, it is possible to highlight the trends of the flow oscillations around the canopy and evaluate them, finding the differences between the various modes.
On $X/D = 6.94$ we are in the wake region of the capsule; starting from there and moving towards the parachute shock wave, we observe a low energy fluctuations zone due to the rebalancing of the flow that closes in correspondence of the shock. For our model, there is nothing between the capsule and the parachute, so the flow moves freely. At $X \approx 8.5$ there is the aforementioned shock: due to the ingestion of incoming turbulence from the shock wave, oscillations begin to increase, producing instabilities that further destabilize the shock position. The most important and critical region is the one preceding the canopy shock wave and the one following it, up to the inside of the parachute. The perturbation generated by capsule on the canopy shock causes the breathing cycle of the parachute; in fact, the capsule wake interacts with the bow shock, changing its position dynamically.
As we can see, the biggest energy variation is at $X \approx 12$, at the start of fully developed wake, after the vent exit; here we get a normal shock wave (in the form of a Mach disk at the exit of a nozzle[1]) which further disrupts the flow together with the wake. Successively, the parachute wake gradually develops as it travels towards the outflow and the oscillations assume a trend similar to a somewhat periodic sinusoidal function at higher flow modes (mode 9 and 10 in particular).

3.2 Pod - Les comparing

The goal of this work is to validate the POD analysis, in order to show how POD data analysis can provide proper reconstruction of flow unsteady dynamics related to the parachute instability. To do this, we use the results given by Large Eddy Simulation (LES) computed using STREAmS. In figure 3.5 it was chosen to show three of the 150 snapshots (snapshots correspond to non-dimensional times t/t_0, so snapshot 24 (e.g.) corresponds to $t/t_0 = 24$) of the POD and compare them with the same LES snapshots: the first (0), the last (149) and the middle one (74). We have chosen to show the velocity parameter because it allows to better appreciate the flow around the parachute.

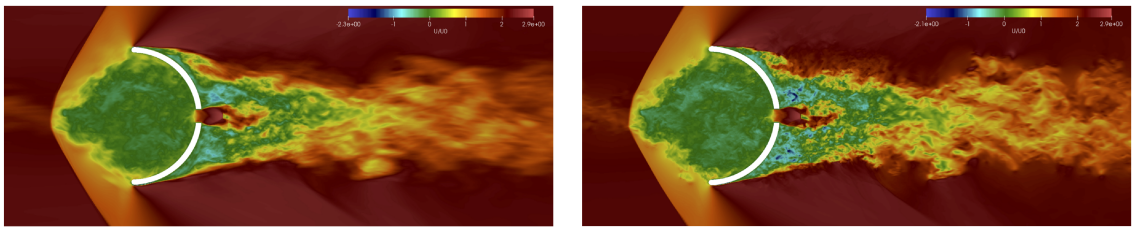

(a) Snapshot 0 POD (b) Corresponding LES snapshot 0

Figure 3.5: POD vs LES snapshots comparing at three different dimensionless times: snapshot 0, snapshot 74 and snapshot 149.

[1]For further details about nozzle behavior, see [4].

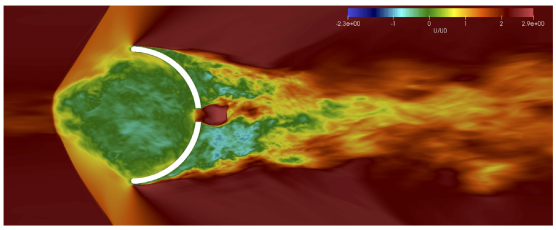

(c) Snapshot 74 POD

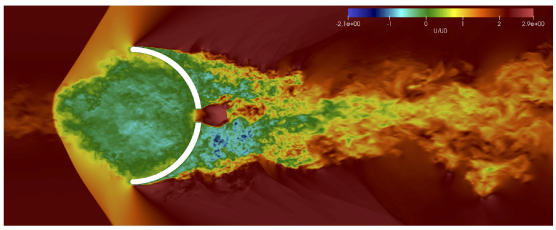

(d) Corresponding LES snapshot 74

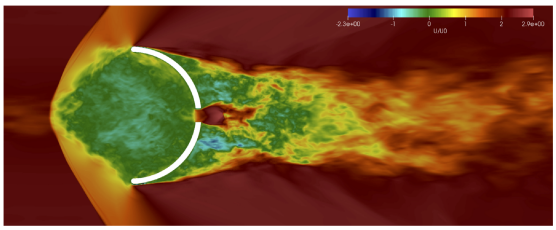

(e) Snapshot 149 POD

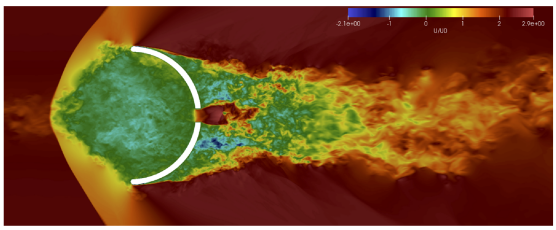

(f) Corresponding LES snapshot 149

Figure 3.5: POD vs LES snapshots comparing at three different dimensionless times: snapshot 0, snapshot 74 and snapshot 149.

First, we focus on the data range scales of LES and POD. It notes that the upper and lower limits of data scales, which correspond to the maximum and minimum non-dimensional velocity values, are very close to each other. This result gives a first validation to the solution since there are no outliers that taint the solution.
The most important detail in these figures is the similarity in the after-shock region: the big vortex structures follow the same pattern of recirculation. However all the small vortexes connected to higher frequencies dynamics are truncated by the POD reconstruction, smothering and dampening the small scales of turbulence. We furtherly study this behaviour by considering the one-dimensional profiles of the reconstructed POD quantity along the x-direction.

Pictures (a), (b) and (c) of figure 3.6 correspond respectively to the cases (a) - (b), (c) - (d) and (e) - (f) of figure 3.5. In order to obtain these plots, we evaluated the velocity along the X domain, on the horizontal line corresponding to $Z = 0$.
First, we note the similarity between POD and LES velocity field for each graph: POD reconstruction is really close to the LES. However, POD does not strictly follow the reference values because of the imposed cap on the higher frequencies given by the fixed number of POD modes selected for the reconstruction.

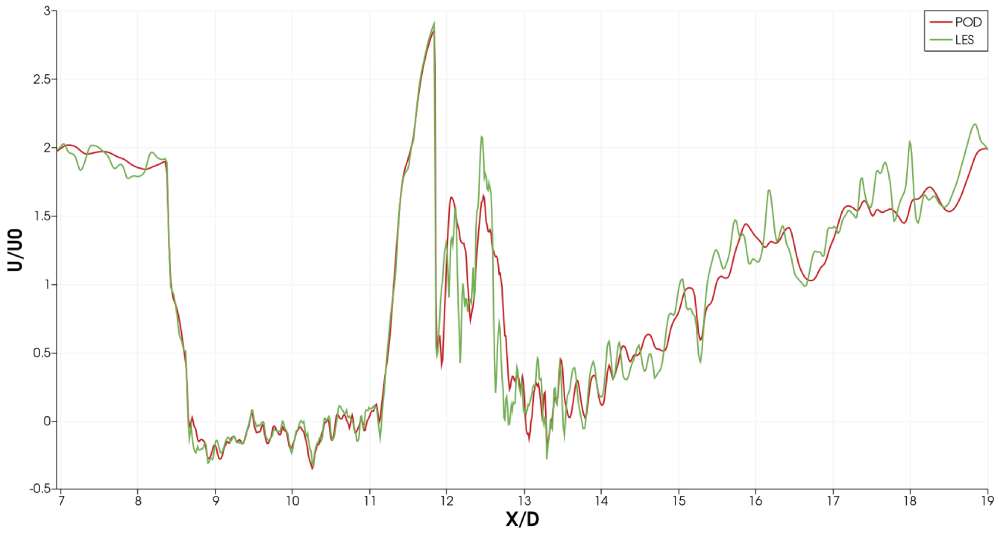

(a) Snapshot 0 - graph

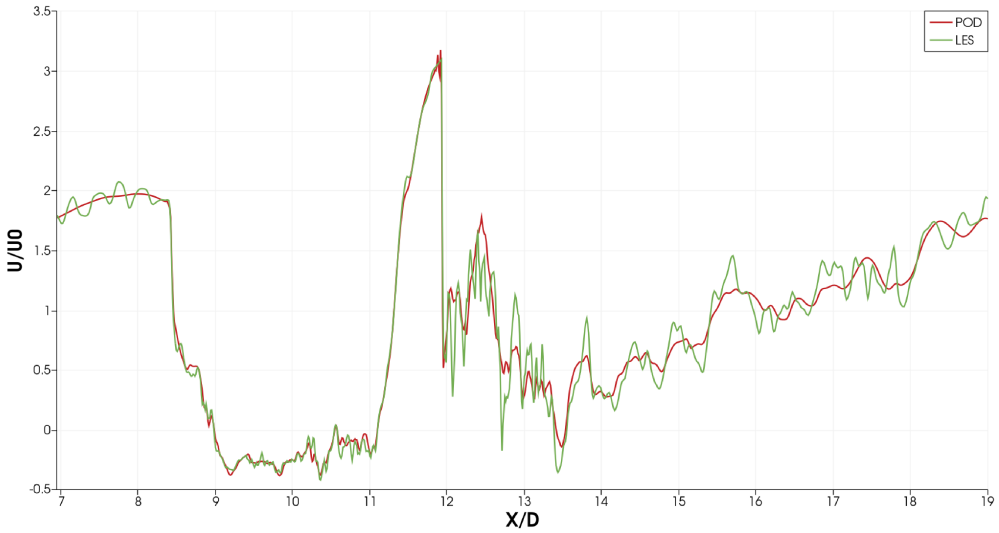

(b) Snapshot 74 - graph

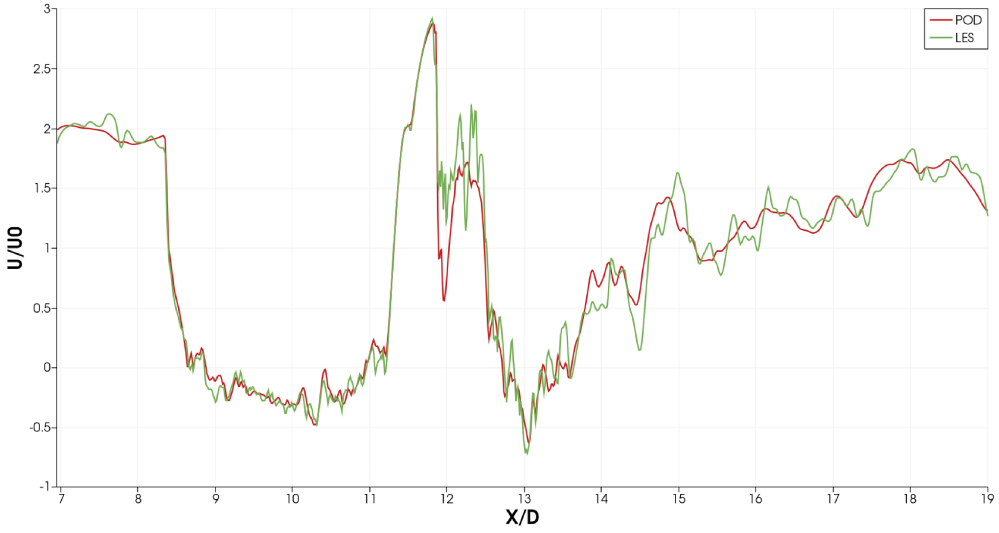

(c) Snapshot 149 - graph

Figure 3.6: POD vs LES for Z/D = 0

Another way to explain the phenomenon is that we can assume POD reconstruction as an averaged field with the addition of the super-imposed flow oscillations: each mode corresponds to a set of frequencies with the same energy content, which are added to the averaged field. The velocity represented on the vertical axis is normalized with respect to a reference quantity; thus all the velocities in this thesis are always express as U/U_0, with U which is the free-stream velocity. We can also define a reference time as:

$$t_0 = \frac{L_0}{U_0} = \frac{D_0\sqrt{\gamma}}{a_\infty} \tag{3.1}$$

where:

- D_0 is the reference length;
- U_0 is the reference velocity;
- γ is the specific heat ratio;
- $a_\infty = 235.40\ m/s$, is the free stream-speed of sound (from ExoMars database).

Another interesting comparison to validate the POD reconstruction consist of analize the LES and POD velocity along the Z-axis. In particular, we took snapshots of the velocity trend, as we did before, for three non-dimensional times: snapshot 0 (first), snapshot 74 (middle one) and snapshot 149 (last). In figure 3.7 we can easily see the transversal sections where velocity has been evaluated.

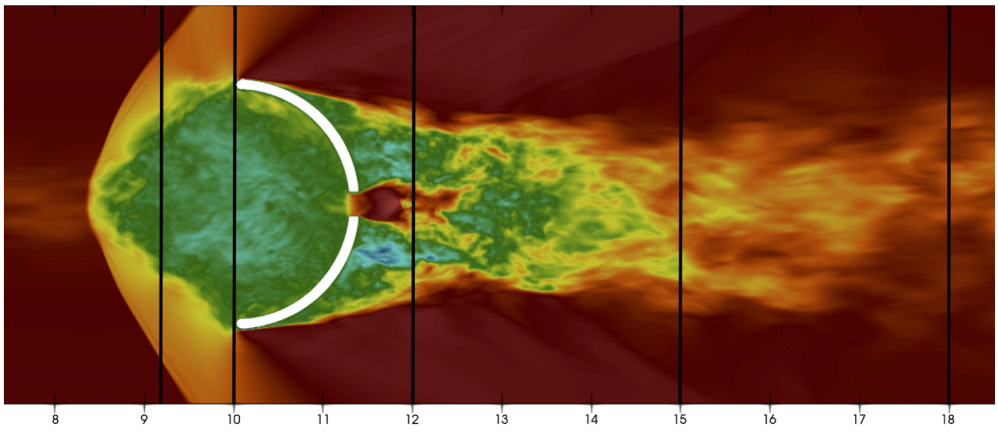

Figure 3.7: X/D sections on which velocity is assessed.

This first case, shown in figure 3.8, is almost symmetric; the discontinuity however widens the portion of recirculation as it travels towards the parachute and fills the canopy volume. In each plot of the aforementioned figure, the most symmetrical zone is located at the extremes of it. We see the velocity jump due to the shock at $Z/D \approx \pm 1.70$ and in particular we observe that POD reconstruction still follows the LES flow oscillations accurately. Behind the shock wave there is an initial zone where the profile shows smaller fluctuations and an almost symmetrical distribution, until we get to the wake region (for $Z/D \approx \pm 0.9$), where

oscillations starts. The promising result of the POD can be appreciated in this figure (as well as in the next ones) because it exhibits the oscillations of the LES profiles even in the wake area, despite showing more limited amplitudes of oscillations.

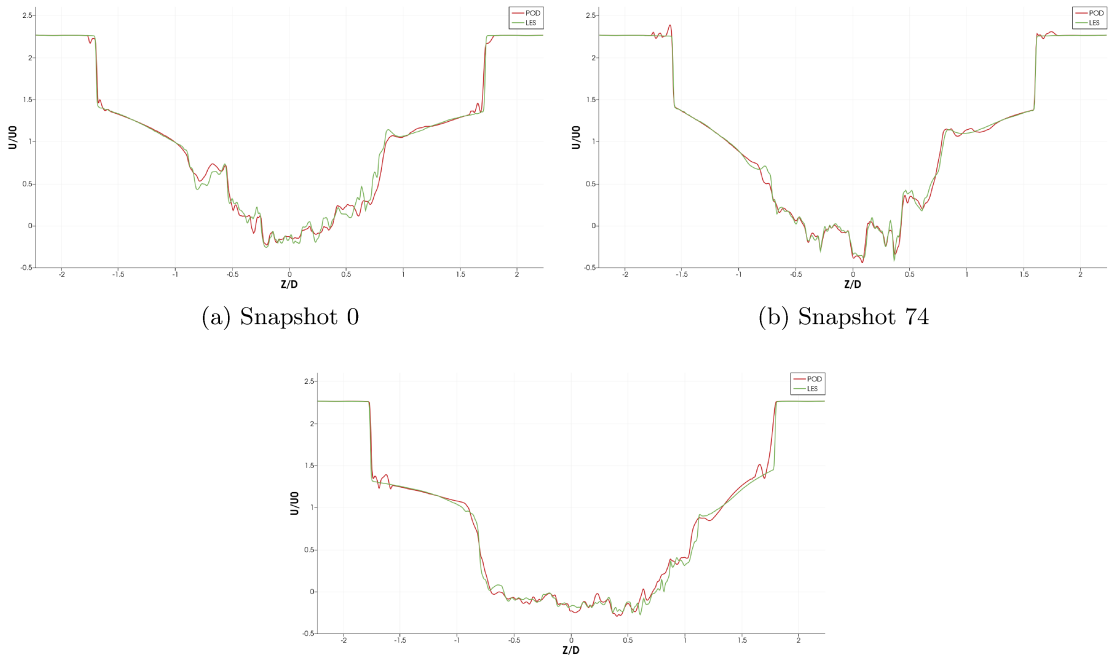

(a) Snapshot 0

(b) Snapshot 74

(c) Snapshot 149

Figure 3.8: POD vs LES for X/D = 9.2

We now repeat this work for specific X-positions; the positions are:

1. $X/D = 10$;
2. $X/D = 12$;
3. $X/D = 15$;
4. $X/D = 18$.

Figure 3.9 below represents the streamwise velocity U/U_0 along a line located at $X/D = 10$, that is the transversal position placed at the inlet of the parachute. In this position, there is a first external zone outside the canopy where there is a decrease in speed (down to zero) due to the approach to the parachute. We have chosen to show these plots with a different velocity range than figure 3.8 to better appreciate the fluctuation of the speed in the wake region: it is clear once again how POD follows LES very closely.

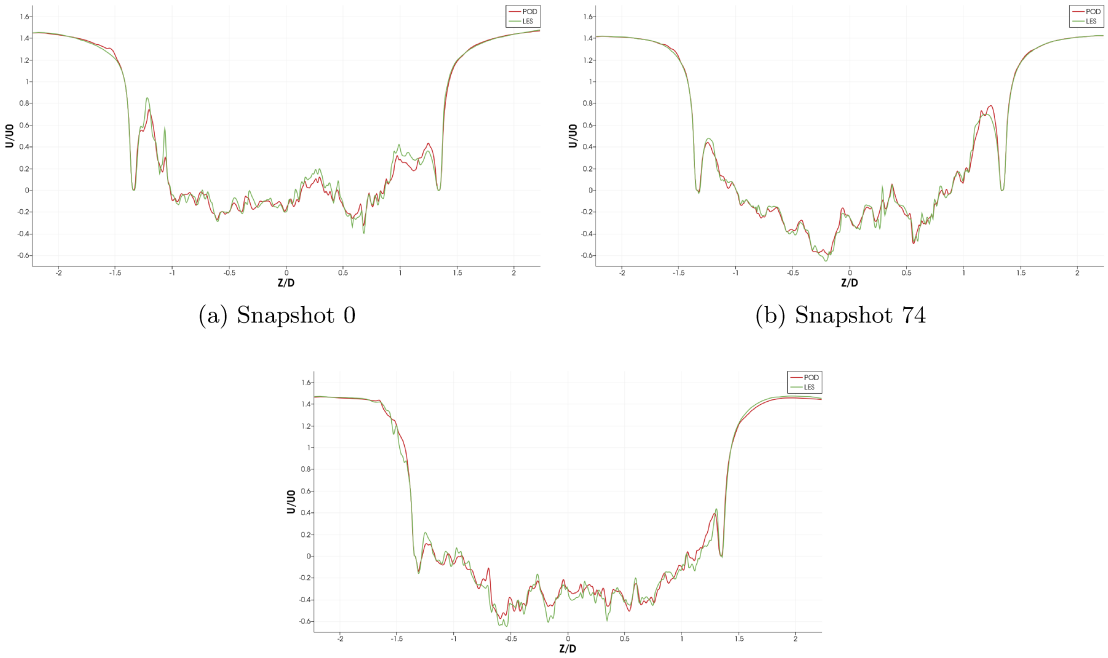

(a) Snapshot 0

(b) Snapshot 74

(c) Snapshot 149

Figure 3.9: POD vs LES for X/D = 10

In figure 3.10 is shown the adimensional velocity at $X/D = 12$. The choice to evaluate U/U_0 here is due to the necessity to get results without the near-wall phenomena at the position corresponding to the outlet of vent (i.e. zero velocity on the wall). As expected, there is a rapid speed increasing at the vent due to the area restriction, as well as explained by convergent-divergent theory [4].

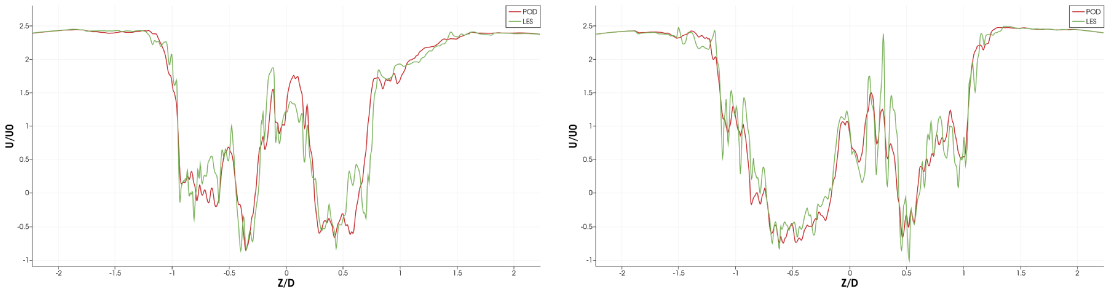

(a) Snapshot 0

(b) Snapshot 74

Figure 3.10: POD vs LES for X/D = 12

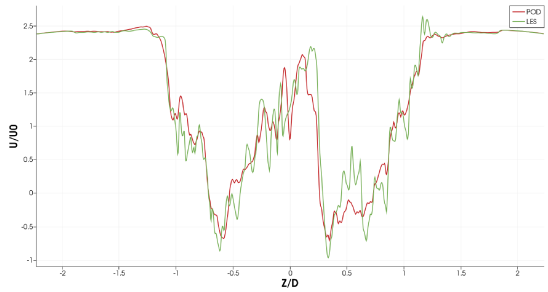

(c) Snapshot 149

Figure 3.10: POD vs LES for X/D = 12

At $X/D = 15$ (figure 3.11) we are in the wake region of the parachute, quite far from the vent. Symmetry in the wake distribution is less apparent here, furthermore, due to the higher intensity in the wake recirculations, POD struggles to follow the LES because the frequency peaks become more intense. These pictures show U/U_0 at $X/D = 15$; in this position, the "symmetry" illustrated above begins to break down and the direction of the primary flow again play a major role on motion in the wake. This point is explained by the vertical axis range: since there is no negative velocities, vortex structures are not strong enough to go against the flow, so the primary one prevails.

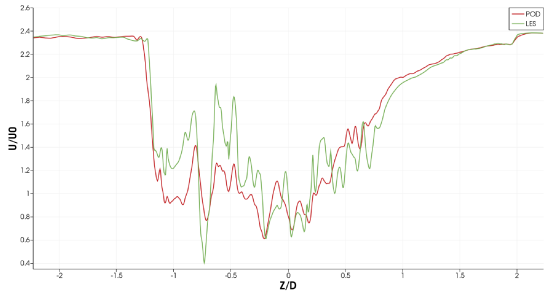

(a) Snapshot 0

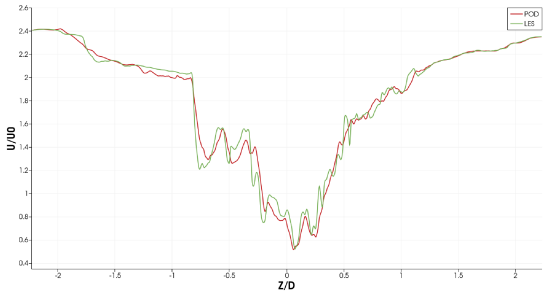

(b) Snapshot 74

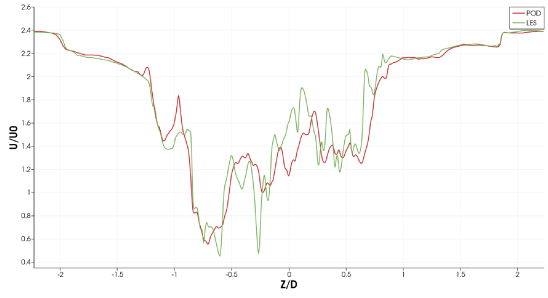

(c) Snapshot 149

Figure 3.11: POD vs LES for X/D = 15

In the last set of pictures, in figure 3.12, we are close to the end of domain, at $X/D = 18$. Once again there is no symmetry in the flow and we can see that POD follows the LES, cutting off higher frequencies contents in the velocity fluctuations. In particular, our reconstruction

does not follow LES at $Z/D \approx [0, 0.5]$. That result may be considered an outlier because it is the only one which does not follow the LES. Thus, POD evaluates the flow behavior very well, even in worst conditions (such as in supersonic wake regions), providing accurate results.

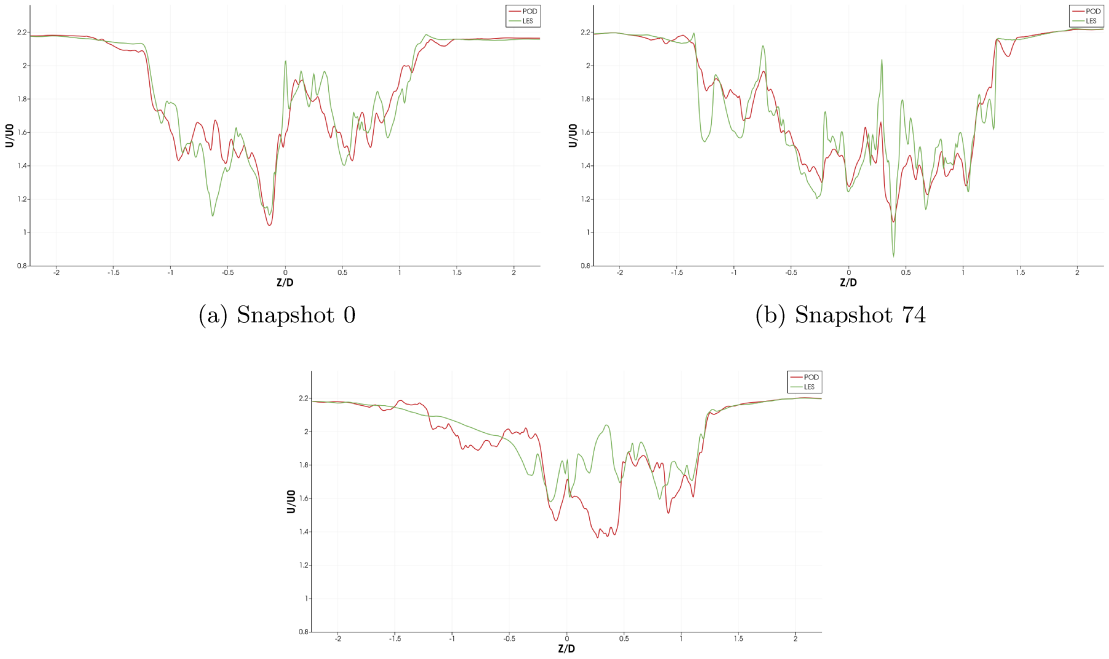

(a) Snapshot 0

(b) Snapshot 74

(c) Snapshot 149

Figure 3.12: POD vs LES for X/D = 18

After these comparisons between POD and LES along the X-axis, it is interesting to evaluate the root mean square of the streamwise velocity field obtained via the POD technique, in order to highlight the fluctuation peak gap affecting the reconstruction, compared to LES.

3.2.1 Root mean square comparison

In this part of this work we show the results obtain by the root mean square calculation applied to the streamwise velocity field for both the POD and LES. Before going to the outcomes, we recall the evaluation made in the previous sections related to effect of the grid distortion on the obtained results. (see footnote 10 at 2.4.3.1 paragraph).
To strive for better results, we try to consider the size of the cell area by applying the spatial weights W to the covariance matrix. Being the outcomes obtained unsatisfactory, we decided to omit those results discarding the erroneous data. Further work is required for future implementation in order to assess the weight connected to the grid distortion effect on the average flow oscillations evaluated via the computation of the RMSs.
The following pictures show the dimensionless RMS velocity (U_{rms}/U_0), calculated along the X-axis, for three different X/D positions: 8, 12 and 16.

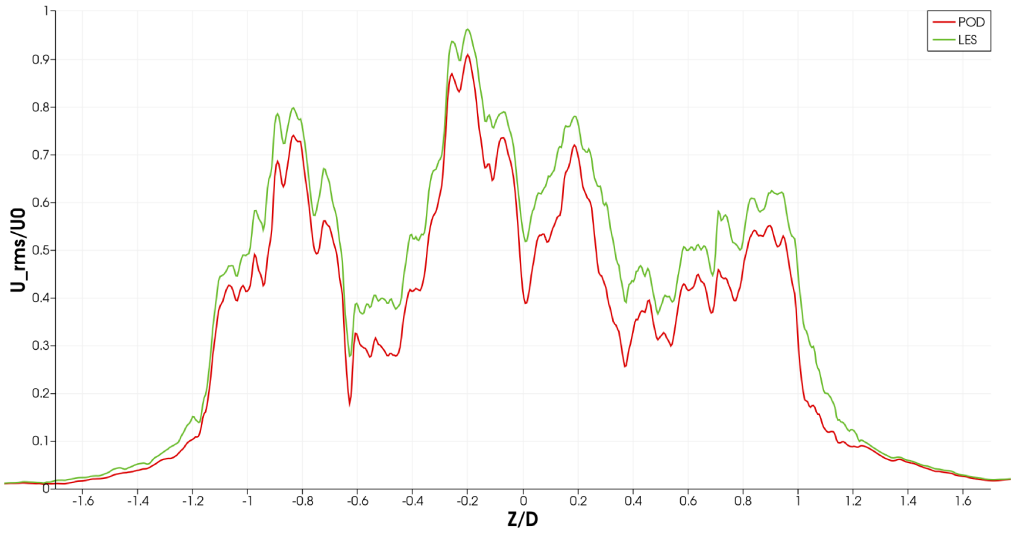

(a) X/D = 8

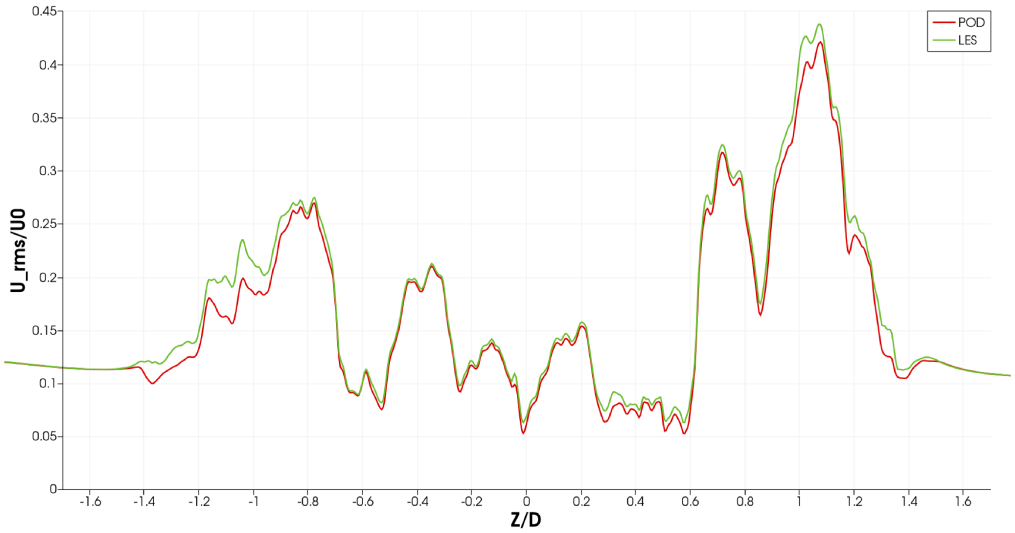

(b) X/D = 12

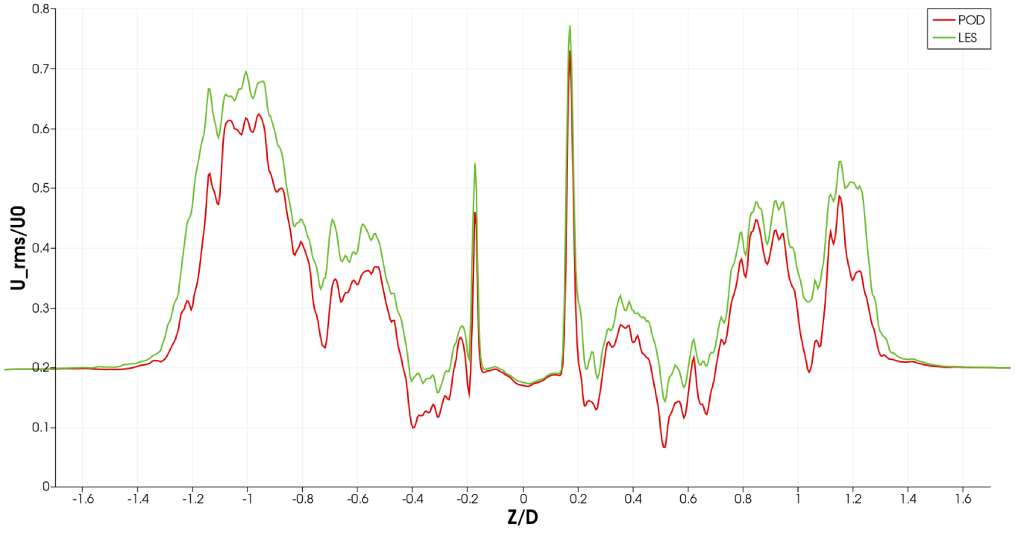

(c) X/D = 16

Figure 3.13: Comparison between POD and LES non-dimensional RMS velocity at different X/D position.

For each case we chose to evaluate the RMS at snapshot 0. In the first case (figure 3.13(a)), the trend of the velocity fluctuations are calculated before the parachute shock-wave: as expected, POD peaks are lower than the LES ones[2] and they are mainly developing in the $Z/D = \pm 1.2$ range. This is due to the fact that, on this position, there is the capsule wake which causes fluctuations in the field; also the RMS peaks are higher than the other cases, since the amplitudes connected to higher frequencies of oscillations are cut out from the reconstruction given by the POD. In figure 3.13(b), U_{rms}/U_0 is calculated forthwith after of the normal shock-wave due to the vent. At $X/D = 12$, POD RMS shows close resemblance with the peak position to LES RMS; these peaks, compared to figure 3.13(a), have a lower amplitude due to the position on the X-axis. Note that those higher values are located on different Z/D: this is clearly owed to the unsteady behavior of the turbulence in the wake regions and to the normal shock-wave; in particular, "vent-shock" reduces velocity without allowing too much fluctuations. We attribute the closer resemblance of the two profiles to the lower quantity of high frequency content in the recirculation patterns. In the last picture of figure 3.13, we evaluate the fluctuations in the fully developed wake region, at $X/D = 16$; once again peaks are located on different position (compared to previous cases), but they begin to regain intensity since higher frequency contents develop as the flow traverses the recompression shock behind the parachute.

[2]The reason of lower peak values is the same of the figure 3.6: POD stores only a percentage of the all energy content (more than 74% in our case), so we get a solution quicker, but we have to accept a lower accuracy. Anyway, the resolution of the reconstruction is high and trustworthy.

4 | Conclusion

This work has been drafted with the intention to evaluate the efficiency of modal analysis techniques applied to supersonic turbulent flows. In particular, we employ Proper Orthogonal Decomposition on the results obtained from the Large Eddy Simulation of a supersonic rigid parachute trailing behind a descent capsule. The technique provided satisfactory results when applied to the simulated flow field. Specifically, we observe how a limited amount of energy modes extracted from the POD analysis (more precisely, ten modes) are able to provide a fairly high amount of the total energy (more than 74%) compared to the starting flow. This allow us to obtain an accurate representation of the original flow field using the reconstructed dynamics. We observe how energy fluctuations (related to the turbulent kinetic energy of the flow) follow the expected wake multiscale dynamics, as pattern of recirculations connected to larger energy contents also correspond to cycles of lower frequencies and smaller regions instead are related to higher frequencies but are associated to a lower intensity. The fidelity in the reconstruction of the dynamics is furtherly explored in the one-dimensional profiles along X and Z directions.

To better evaluate the overall precision in representing the dynamics of oscillations around the canopy over time, root mean square profiles of reconstructed quantity have been compared with the original LES RMS time-averaged fluctuations. Once again, it has been observed a close resemblance of the profiles, despite the existence of a very small gap in the intensity caused by the excluded POD modes.

Proper orthogonal decomposition, together with other modal analysis methods, might become an important aid in the foreseeable future of computational fluid dynamics given its capability to provide an immediate insight in the dynamics of complex turbulent flows. The data analysis performed shows how it can become an excellent candidate for approaching via low order modeling the flow unsteadiness. The results obtained can be potentially implemented in static aerodynamic databases to aid in the description of the flight instabilities related to parachute oscillations that contribute to the deviation from the nominal reentry trajectory of the probe. Further development on the subject can involve the use of different modal analysis techniques such as Dynamic Mode Decomposition or the implementation of machine learning strategies [14] [22] to additionally improve the extrapolative capabilities of a connected flow model.

Bibliography

[1] A. Aboudan, G. Colombatti, C. Bettanini, F. Ferri, S. Lewis, B. Van Hove, O. Karatekin, S. Debei. *"ExoMars 2016 Schiaparelli module trajectory and atmospheric profiles reconstruction"*, In: Space Science Reviews 214.5 (2018), pp. 1–31.

[2] J. D. Anderson Jr. *"Fundamentals of Aerodynamics"*, 5^{th} ed., McGraw-Hill, 2010, pp. 908-923.

[3] M. Barnhardt, T. Drayna, I. Nompelis, G. Candler, W. Garrard. *"Detached eddy simulations of the MSL parachute at supersonic conditions"*, In: 19^{th} AIAA Aerodynamic Decelerator Technology Conference and Seminar, Williamsburg, VA, USA, 2007.

[4] E. Benini. *"Propulsione Aerea"*, 2^{nd} ed., Cleup, April 2014 pp. 249-251.

[5] G. Berkooz, P. Holmes, J. L. Lumley. *"The Proper Orthogonal Decomposition in the Analysis of Turbulent Flows"*, In: Annu. Rev. Fluid Mech. Vol. 25, No. 1, 1993, pp. 539–575.

[6] M. Bernardini, D. Modesti, F. Salvadore, and S. Pirozzoli. *"STREAmS: A high-fidelity accelerated solver for direct numerical simulation of compressible turbulent flows"*, In: Computer Physics Communications 263 (2021), p. 107906.

[7] J.R. Cruz. *"Parachutes for planetary entry systems"*, In: ed. by NASA Langley Research Center, 2005.

[8] J.R. Cruz, C. O' Farrell, E. Hennings, P.Runnells. *"Permeability of two parachute fabrics - Measurements, modeling, and application"*, In: NASA/TM-2016-219328 (Corrected Copy), 2016.

[9] J.R. Cruz, D. Way, J. Shidner, J.L. Davis, R.W. Powell, D. Kipp, D.S. Adams, A. Sengupta, A. Witkowski, and M. Kandis. *"Parachute models used in the Mars Science Laboratory entry, descent, and landing simulation"*, In: AIAA Aerodynamic Decelerator Systems (ADS) Conference, 2013, p. 1276.

[10] N. Dahal, K. Fukiba, K. Mizuta, Y. Maru. *"Study of pressure oscillations in supersonic parachute"*, In: International Journal of Aeronautical & Space Sciences (2018) 19:24–31.

[11] F. De Vanna. *"A high-resolution fully compressible Navier-Stokes solver for analysis of moving objects at high Mach numbers"*, PhD thesis, 2019, pp. 35, 84-85.

[12] F. Ducros, V. Ferrand, F. Nicoud, C. Weber, D. Darracq, D. Gacherieu, T. Poinsot. *"Large-Eddy Simulation of the Shock/Turbulence Interaction"*, J. Comput. Phys. 152 (2),1999, 517–549.

[13] F. Ferri, Ö. Karatekin, S.R. Lewis, F. Forget, A. Aboudan, G. Colombatti, C. Bettanini, S. Debei, B. Van Hove, V. Dehant, et al. *"Exomars atmospheric mars entry and landing investigations and analysis (AMELIA)"*, In: Space Science Reviews 215.1 (2019), pp. 1–21.

[14] S. Fresca, A. Manzoni. *"POD-DL-ROM: Enhancing deep learning-based reduced order models for nonlinear parametrized PDEs by proper orthogonal decomposition"*, In: Comput. Methods Appl. Mech. Engrg. 388, 114181, 2022.

[15] A. Hellsten. *"New two-equation turbulence model for aerodynamics applications, Report A-21"*, Helsinki University of Technology, Laboratory of Aerodynamics, 2004, pp. 21-24.

[16] H. Johari, K. J. Desabrais. *"Vortex shedding in the near wake of a parachute canopy"* In: J. Fluid Mech., 2005, vol. 536, pp. 185-207.

[17] K. Karagiozis, R. Kamakoti, F. Cirak, C. Pantano. *"A computational study of supersonic disk-gap-band parachutes using Large-Eddy Simulation coupled to a structural membrane"* In: Journal of Fluids and Structures 27 (2011), pp. 175–192.

[18] R. Mittal, G. Iaccarino. *"Immersed boundary methods"* In: Annu. Rev. Fluid Mech., 37 (2005), p. 249.

[19] A. T. Mohan, D. V. Gaitonde, M. R. Visbal. *"Model reduction and analysis of deep dynamic stall on a plunging airfoil using dynamic mode decomposition"*, In: AIAA SciTech, 53^{rd} AIAA Aerospace Sciences Meeting, 5-9 January 2015.

[20] P. Moin, K. Mahesh *"Direct Numerical Simulation: a tool in turbulence research"*, Annu. Rev. Fluid Mech., 1998, 30:539–578, pp. 539-543.

[21] S. B. Pope. *"Turbulent Flows"*, Cambridge Univ. Press, 2000, pp. 188, 373-375.

[22] J. Roth. *"Proper orthogonal decomposition for fluid mechanics problems"*, Master thesis, 2021, pp. 53-54.

[23] C. W. Rowley, S. T. M. Dawson. *"Model reduction for flow analysis and control"*, In: Annu. Rev. Fluid Mech. 2017, 49:387-417, p. 388.

[24] A. Sengupta. *"Fluid structure interaction of parachutes in supersonic planetary entry"*, In: AIAA Paper 2011-2541, 2011.

[25] G. Soldati. *"Numerical investigation of the parachute-capsule aerodynamics in a Mars atmosphere reentry"*, MSC thesis, 2022, pp. 13-23.

[26] K. Taira, S. L. Brunton, S. T. M. Dawson, C. W. Rowley, T. Colonius, B. J. McKeon, O. T. Schmidt, S. Gordeyev, V. Theofilis, L. S. Ukeiley, *"Modal analysis of fluid flows: an overview"*, In: AIAA journal, Vol. 55, No. 12, December 2017, p. 4015-4018, 4020-4023.

[27] T. Tolker-Nielsen. *"ExoMars 2016 - Schiaparelli anomaly inquiry"*, Report. European Space Agency, 2017.

[28] J. L. Vago (SCI-S). *"ExoMars 2022 mission. Brief description of the rover and surface platform"*, In: European Space Agency unclassified, Document, 30 November 2020, pp. 5-6.

[29] J. R. Wright, J. E. Cooper. *"Introduction to aircraft aeroelasticity and loads"*, 2^{nd} ed., John Wiley & Sons, 2015, pp. 30, 34.

[30] X.P. Xue, H. Koyama, Y. Nakamura, and C.Y. Wen. *"Effects of suspension line on flow field around a supersonic parachute"*, In: Aerospace Science and Technology 43 (2015), pp. 63–70.

[31] X. Xue, C. Y. Wen. *"Review of unsteady aerodynamics of supersonic parachutes"*, In: Progress in Aerospace Sciences 125 (2021), 100728, pp. 3-4, 15, 22-23.